SARS-CoV-2 spike-glycoprotein processing at S1/S2 and S2' and shedding of the ACE2 viral receptor: roles of Furin and TMPRSS2 and implications for viral infectivity and cell-to-cell fusion

Rachid Essalmani[1], Jaspreet Jain[2,7], Delia Susan-Resiga[1,7], Ursula Andréo[1,2,7], Alexandra Evagelidis[1], Rabeb Mouna Derbali[1], David N. Huynh[1], Frédéric Dallaire[2], Mélanie Laporte[2], Adrien Delpal[3], Priscila Sutto-Ortiz[3], Bruno Coutard[4], Claudine Mapa[5], Keith Wilcoxen[5], Etienne Decroly[3], Tram NQ Pham[2], Éric A. Cohen[2,6*] & Nabil G. Seidah[1*]

[1] **Laboratory of Biochemical Neuroendocrinology Montreal Clinical Research Institute** (IRCM, affiliated to the Univ. of Montreal) 110 Pine Ave west, Montreal, QC, H2W1R7, Canada

[2] **Laboratory of Human Retrovirology Montreal Clinical Research Institute** (IRCM, affiliated to the University of Montreal) 110 Pine Ave west, Montreal, QC, H2W1R7, Canada

[3] **AFMB, CNRS**, Université Aix-Marseille, CNRS, UMR 7257, Case 925, 163 Avenue de Luminy, 13288 Marseille Cedex 09, France, Marseille, France

[4] **Unité des Virus Émergents** (UVE: Aix-Marseille Univ - IRD 190 - **Inserm** 1207 - IHU Méditerranée Infection), Marseille, France

[5] **Boston Pharmaceuticals,** Translational Research, 55 Cambridge Parkway, Suite 400, Cambridge, MA 02142, USA

[6] **Department of Microbiology, Infectiology and Immunology**, Université de Montréal, Montréal, Québec, Canada

[7] Each of these authors contributed equally: Jaspreet Jain, Delia Susan-Resiga and Ursula Andreo

[*]Corresponding authors: seidahn@ircm.qc.ca; eric.cohen@ircm.qc.ca

Short title: **Furin & TMPRSS2: spike cleavage & SARS-CoV-2 infection**

ABSTRACT

The spîke (S)-protein of SARS-CoV-2 binds ACE2 and requires proteolytic "priming" at P**R**RA**R**$_{685}$↓ into S1 and S2 (cleavage at S1/S2), and "fusion-activation" at a S2' site for viral entry. *In vitro,* Furin cleaved peptides mimicking the S1/S2 cleavage site more efficiently than at the putative S2', whereas TMPRSS2 inefficiently cleaved both sites. In HeLa cells Furin-like enzymes mainly cleaved at S1/S2 during intracellular protein trafficking, and S2' processing by Furin at KPS**KR**$_{815}$↓ was strongly enhanced by ACE2, but not for the optimized S2' KRRKR$_{815}$↓ mutant (μS2'), whereas individual/double KR815AA mutants were retained in the endoplasmic reticulum. Pharmacological Furin-inhibitors (Boston Pharmaceuticals, BOS-inhibitors) effectively blocked endogenous S-protein processing in HeLa cells. Furthermore, we show using pseudotyped viruses that while entry by a "pH-dependent" endocytosis pathway in HEK293 cells did not require Furin processing at S1/S2, a "pH-independent" viral entry in lung-derived Calu-3 cells was sensitive to inhibitors of Furin (BOS) and TMPRSS2 (Camostat). Consistently, these inhibitors potently reduce infectious viral titer and cytopathic effects, an outcome enhanced when both compounds were combined. Quantitative analyses of cell-to-cell fusion and spîke processing revealed the key importance of the Furin sites for syncytia formation. Our assays showed that TMPRSS2 enhances fusion and proteolysis at S2' in the absence of cleavage at S1/S2, an effect that is linked to ACE2 shedding by TMPRSS2. Overall, our results indicate that Furin and TMPRSS2 play synergistic roles in generating fusion-competent S-protein, and in promoting viral entry, supporting the combination of Furin and TMPRSS2 inhibitors as potent antivirals against SARS-CoV-2.

IMPORTANCE

SARS-CoV-2 is the etiological agent of COVID-19 that resulted in >5 million deaths. The spike protein (S) of the virus directs infection of the lungs and other tissues by binding the angiotensin-

converting enzyme 2 (ACE2) receptor. For effective infection, the S-protein is cleaved at two sites: S1/S2 and S2'. Cleavage at S1/S2, induces a conformational change favoring the recognition of ACE2. The S2' cleavage is critical for cell-to-cell fusion and virus entry into host cells. Our study contributes to a better understanding of the dynamics of interaction between Furin and TMPRSS2 during SARS-CoV-2 entry and suggests that the combination of a non-toxic Furin inhibitor with a TMPRSS2 inhibitor could significantly reduce viral entry in lung cells, as evidenced by an average synergistic ~95% reduction of viral infection. This represents a powerful novel antiviral approach to reduce viral spread in individuals infected by SARS-CoV-2 or future related coronaviruses.

INTRODUCTION

Epidemics date from prehistoric times but are exacerbated by overcrowding and human impact on the ecosystem (1). The RNA coronaviruses (CoV) are zoonotic pathogens that occasionally spread in the human population, causing respiratory, enteric, renal, and neurological diseases (2). Electron microscopy of CoV revealed that the lipid envelope of each virion is surrounded by a "crown"-like structure (3), composed of multiple copies of a viral surface glycoprotein known as "spike" (S), which is essential for receptor binding and virus entry. Severe Acute Respiratory Syndrome coronavirus (SARS-CoV-1) and Middle East Respiratory Syndrome coronavirus (MERS-CoV) are infectious pathogenic viruses that appeared in humans at the beginning of the 21st century (2, 4). At the end of 2019, a third CoV, namely SARS-CoV-2, emerged causing widespread respiratory and vascular illnesses (5), coined COVID-19 (6).

Like envelope glycoproteins of many infectious viruses (7-9), the secretory type-I membrane-bound S of SARS-CoV-2 is synthesized as a precursor (proS) that undergoes post-transcriptional cleavages by host cell proteases at specific sites to allow viral entry. During infection, the trimeric proS (monomer, 1,272 residues) is first processed at an S1/S2 cleavage site (Fig. 1A). Unlike SARS-CoV-

1, the S-protein of SARS-CoV-2 exhibits an insertion of four critical amino acids (PRRA) at the S1/S2 junction (10-12), forming a canonical P**R**RA**R**$_{685}$↓ Furin-like cleavage site (FCS). Such "priming" step divides the protein into two subunits S1 and S2 held together by non-covalent interactions. Following S-protein priming, the N-terminal S1-ectodomain undergoes a conformational change that exposes its receptor-binding-domain (RBD) (13), which recognizes the ACE2 entry receptor (11). The S2-subunit, which is responsible for the fusogenic activity of the spike-S glycoprotein, contains an additional "fusion-activation" proteolytic site (S2') followed by an α-helical fusion peptide (FP) and two heptad-repeat domains (HR1 and HR2) preceding the transmembrane domain (TM) and cytosolic tail (CT) (Fig. 1A). It is thought that cleavage at S2' triggers large-scale rearrangements, including a refolding step that is associated with the separation of S1- and S2-subunits and exposure of the hydrophobic α-helix FP, favoring fusion of viral and host cell membranes leading to virus entry (14). Fusion with host cells can occur either at the cell surface (pH-independent) or with internal membranes following endocytosis (pH-dependent) (15). However, the cognate host-cell proteases responsible for the S1/S2 and S2' cleavages vary between coronaviruses and cell types (11, 12, 16-19).

The proprotein convertases (PCs; genes *PCSKs*) constitute a family of nine secretory serine proteases that regulate various processes in both health and disease states (20). Through proteolysis, PCs are responsible for the activation and/or inactivation of many secretory precursor proteins, including virus/pathogen surface glycoproteins (9, 20). Seven PCs, including the widely expressed Furin, PC5A, PACE4 and PC7, cleave secretory substrates at specific single/paired basic amino acids (aa) within the motif (K/R)-X_n-(K/R)↓, where Xn= 0, 2, 4 or 6 spacer X residues (20). Because of their critical functions, PCs, especially Furin (21), are implicated in many viral infections by inducing specific cleavages of envelope glycoproteins, a condition that allows not

only the fusion of the viral lipid envelope with host cell membranes (9, 20), but can also lead to cell-to-cell fusion (syncytia), especially for viruses that undergo pH-independent fusion (22, 23).

As the S1/S2 cleavage of SARS-CoV-2 is thought to play a critical role for cellular receptor recognition and virus entry, the efficacy and extent of this activation step by host proteases might be a key determinant regulating cellular tropism, viral pathogenesis, and human-to-human transmission. In contrast to SARS-CoV-1, the proS of SARS-CoV-2 contains a structurally exposed P**R**RA**R**$_{685}$↓S**V** motif (10, 11) (Fig. 1A), which corresponds to a canonical FCS (9, 10, 20). This Furin-like motif is presumably cleaved during *de novo* virus egress (23) for S-protein priming and may play a key role for the efficient spread of SARS-CoV-2 to various human tissues compared to the more limited tropism of other lineage B β-coronaviruses (10, 24). Furthermore, based on the predicted S2' KPS**KR**$_{815}$↓S**F** sequence of SARS-CoV-2, we proposed (10) that Furin-like enzymes could also cleave at this S2' site (Fig. 1A). Indeed, various reports have since supported the implication of Furin in the S1/S2 priming of the S-protein in human cell culture models (12, 25, 26) and *in vivo* in mice, hamsters and ferrets (27, 28). In addition, it was also suggested that the cell surface type-II transmembrane serine protease 2 (TMPRSS2) can enhance fusion by cleavage at S2', but that S1/S2 cleavage is mostly Furin-dependent (18). The ability of the Arg/Lys-specific TMPRSS2 (29, 30) to directly cleave at S2' was suggested based on the viral entry blockade by the TMPRSS2 inhibitor Camostat (31-33), and through silencing of TMPRSS2 expression using a morpholino oligomer (18), but direct evidence of its involvement in such spike protein processing at S2' is still lacking. Thus, it is likely that one or more proteases regulate SARS-CoV-2 entry into human airway epithelial cells (18, 24). Furthermore, since the tissue-expression of TMPRSS2 is restricted to a limited set of cell types compared to that of the ubiquitously expressed Furin, the activity of the latter may widen viral tropism (34).

Thus, the major goals of the present study were to precisely define the respective roles of Furin and TMPRSS2 in the fusion activation, and to test the consequences of their inhibition on SARS-CoV-2 infectivity and S-mediated cell-to-cell fusion. Herein, using a multi-disciplinary approach, we provide mechanistic evidence supporting a critical role of the proprotein convertase Furin in the processing of SARS-CoV-2 spike protein. Specifically, we map the exact S2' processing site by proteomics and highlight by mutagenesis the functional importance of S1/S2 and S2' regions in viral entry and cell-to-cell fusion. For the first time, we demonstrate that three novel cell-permeable small molecules inhibitors of proprotein convertases developed by Boston Pharmaceuticals, referred hereafter as BOS-inhibitors, can potently inhibit proS processing at S1/S2 and S2' by endogenous Furin-like proteases leading to efficient inhibition of viral entry, viral replication, and cell-to-cell fusion. Finally, our work sheds a new light on the role of TMPRSS2 in promoting ACE2 shedding and enabling S2' processing, thereby leading to enhanced cell-to-cell fusion.

RESULTS

Comparative analysis of cleavage of SARS-CoV-2 peptides mimicking S1//S2 and S2' processing sites by Furin and TMPRSS2. Furin is thought to be important in the processing of SARS-CoV-2 spike-glycoprotein (S) at the S1/S2 site (10, 24) while TMPRSS2 has been proposed to have an important role in activating S at S2' (18, 31-33) (Fig. 1A). Nevertheless, the relative contributions of Furin and TMPRSS2 towards cleavage of SARS-CoV-2 S glycoprotein at both sites remain poorly defined. Thus**,** the susceptibility of SARS-CoV-2 S glycoprotein to Furin-cleavage was first assessed *in vitro*. Incubation of quenched fluorogenic peptides encompassing S1/S2 and S2' sites (Supporting Information SI-Table 1) demonstrated that the S1/S2 site of SARS-CoV-2 S was efficiently cleaved by 2 nM Furin at pH 7.5 (Fig. 1B), whereas the S1/S2 site of SARS-CoV-1, which lacks an FCS, was not cleaved (Fig. 1B). Furin less efficiently cleaved the SARS-CoV-2-mimic

peptide at S2', requiring 50-fold higher enzyme concentrations (100 nM) to detect cleavage (inset Fig. 1B). The high specificity of the SARS-CoV-2 for processing at Furin-like motifs was next confirmed by demonstrating that substitutions of basic residues at the S1/S2 cleavage site (RRA**A**$_{685}$↓S, **A**RA**A**$_{685}$↓S, **A**RAR$_{685}$↓S) dramatically impaired S1/S2 cleavage (Fig. 1B). Altogether, these data demonstrate that *in vitro* Furin best cleaves at S1/S2 and less efficiently at S2'. In contrast, TMPRSS2 did not efficiently cleave the S1/S2 and S2' peptides (Fig 1C). The cleavage at S1/S2 became detectable only when TMPRSS2 was present at high concentration (50 nM). However, different from Furin, under this condition TMPRSS2 cleavage of peptides mimicking the S1/S2 Ala-mutants RRAA, ARAA and ARAR and S2' was also evident (Fig. 1C). Taken together, these data emphasize the critical importance of the P1 and P4 Arg for Furin-mediated cleavage at S1/S2 and suggest that the likely Arg-motif recognized by TMPRSS2 is either (Ala/Arg)-Arg↓Ala or Ala-Arg↓Ser with a preference for Ala at P2 over Arg, and Ala or Ser at P1'.

Furin and Furin-like proteases can process proS at S1/S2 and S2' sites. To examine the ability of Furin and Furin-like enzymes to process the precursor proS of SARS-CoV-2 *in cellulo,* we used a HeLa cells model, which endogenously express Furin but not TMPRSS2 or ACE2 (*not shown*), as reported earlier (35). Here, we found that endogenous enzymes efficiently processed a V5-tagged proS (Fig. 1A), likely at the S1/S2 junction to generate a ~100 kDa S2-like fragment (Fig. 2A). Interestingly, when the proprotein convertases PC5A, Furin, PC7 or PACE4 were transiently overexpressed, cleavage at this site became more prominent. Of note, a partial knockdown of Furin decreased S2 levels by more than 60% (SI-Fig. 1A). Furthermore, it was only when Furin or PC5A were overexpressed that cleavage at a potentially S2' site was noticeable, yielding a ~75 kDa fragment (Fig. 2A). The remaining ~200 kDa proS$_{im}$ corresponded to an immature precursor form that had not exited the ER, as attested by its sensitivity to both endoglycosidase-F and endoglycosidase-H (SI-Fig. 1B)

and insensitivity to Furin-like convertases, which are only active in the TGN and/or cell surface/endosomes (20, 36).

To precisely define the ~100-kDa fragment, we mutated the S1/S2 site **R**RA**R**$_{685}$↓S and found that the double Ala-mutant [**A**RA**A**$_{685}$] (denoted μS1/S2) abrogated processing at S1/S2 and putative S2' (Fig. 2B), highlighting once again the importance of the P4- and P1-Arg for recognition by Furin-like enzymes (20). The loss of Furin-like cleavage at S1/S2 resulted in accumulation of a higher molecular size band (~230 kDa), representing mature proS, that exited the endoplasmic reticulum (ER), as confirmed by its resistance to endoglycosidase-H, while still sensitive to endoglycosidase-F digestion (SI-Fig. 1B).

To further define the Arg-residues critical for processing at S1/S2, we assessed the effect of single residue mutations: R682A, R685A and S686A and confirmed the critical importance of P1-Arg$_{685}$ or P4-Arg$_{682}$ for the generation of S2 by endogenous Furin (SI-Fig. 1C). However, unlike μS1/S2 (Fig. 2B), these single mutants were partially cleaved by overexpressed Furin (SI-Fig. 1C), reflecting the multi-basic nature of the S1/S2 recognition sequence and suggesting the importance of the P3 Arg$_{683}$ (37). The S686A mutant was based on the prediction that Ser$_{686}$ could be O-glycosylated (38), which may hamper processing at S1/S2 (39). However, like the WT-S, the S686A mutant was efficiently processed by Furin into S2 and S2' (SI-Fig. 1C), suggesting the lack of O-glycosylation at Ser$_{686}$ in HeLa cells.

We next used site-directed mutagenesis to identify the exact S2' site cleaved by Furin. However, K814A, R815A and K814R815A mutants at P1 and P2 residues (20) of the predicted S2' site (KPSKR$_{815}$↓SF) altered S-protein trafficking resulting in a predominantly ER-retained proS$_{im}$ protein, especially for the R815A and the double mutant (SI-Fig. 1D). Therefore, we resorted to mass spectrometry analysis of proteins migrating at the S2' position to unambiguously identify this site. The peptides generated by a Lys-specific protease (K$_{814}$↓) allowed for the discrimination

between SFIEDLLFNK$_{825}$ that would be generated if Furin cleaved at Arg$_{815}$, and R$_{815}$SFIEDLLFNK$_{825}$ that would be derived from N-terminally extended proteins, e.g., S2. Proteomic data (Fig. 2C) revealed a >50-fold higher ratio of SFIEDLLFNK$_{825}$ to RSFIEDLLFNK$_{825}$ for the S2' product, demonstrating that the N-terminus of S2' starts at Ser$_{816}$ and that Furin cleaves after Arg$_{815}$↓ in the sequence KPSK**R**$_{815}$↓SFIEDLLFNKVT (Fig. 1A). To further demonstrate the role of Furin in S2' cleavage we generated a Furin-optimized S2' site (called μS2') with a polybasic sequence KRRKR$_{815}$↓SF in proS and found that this derivative was very efficiently cleaved by endogenous and especially by overexpressed Furin, yielding a similar ~75 kDa fragment (Fig. 2D). Altogether, these data demonstrate that the S2' cleavage occurs at Arg$_{815}$↓ and further reveal that this site can be partially processed by overexpressed Furin and/or PC5A.

Processing at S2' by Furin is enhanced in the presence of ACE2. Immunocytochemical analyses of HeLa cells co-expressing S or μS1/S2-S and ACE2 showed that both S-proteins and ACE2 co-localized at the cell surface independent of the state of proS processing (SI-Fig. 2). Given that binding of SARS-CoV-2 S-trimer to the dimeric ACE2 receptor has been proposed to trigger a conformational change in S1, promoting cleavage at S2' (13, 40), we next examined whether this phenomenon would effectively increase/promote S2' processing by Furin. To this end, we expressed the V5-tagged proS spike protein together with ACE2 and Furin in HeLa cells. We found that while not significantly affecting S1/S2 cleavage, ACE2 expression seemed to stabilize the S2 subunit and to strongly enhance the generation of S2' by endogenous and overexpressed Furin (Fig. 3A). Amazingly, in the presence of ACE2, the μS1/S2-S, which is otherwise resistant to cleavage at S1/S2 by endogenous or overexpressed Furin (Fig. 2B), can be partially cleaved directly into S2' by

213 overexpressed Furin (Fig. 3B, last lane). Taken together, we conclude that binding of S-protein to
214 ACE2 likely facilitates exposure of the S2' site (41), thereby enhancing Furin processing at S2'.
215
216 **Furin-inhibitors block S1/S2 and S2' cleavages.** Given the importance of Furin in proS
217 processing at the S1/S2 and S2' sites, we next evaluated the activity of three novel non-toxic, cell-
218 permeable Furin-like inhibitors developed by Boston Pharmaceuticals available as oral (BOS-981,
219 BOS-318) or inhalable (BOS-857) formulations (Fig. 4A). Accordingly, we first tested *in vitro* the
220 efficacy and selectivity of these inhibitors on purified soluble forms of Furin, PC5A, PACE4 and
221 PC7 using a quenched fluorogenic substrate FAM-Q**R**V**RR**AVGIDK-TAMRA. As shown, the
222 inhibitors effectively blocked substrate processing by all convertases with an IC_{50} of ~7-9 nM
223 compared to ~9-10 nM for the known cell-permeable PC-inhibitor decanoyl-RVKR-
224 chloromethylketone (dec-RVKR-cmk) (42, 43) (Fig. 4B). The Furin S1/S2 cleavage was also
225 validated using a 12-residue quenched fluorogenic substrate DABSYL/Glu-TNSP**RR**A**R**↓SVAS-
226 EDANS mimicking the S1/S2 priming site. The inhibition deduced after hill-plot curve fitting (Fig.
227 4C) gave an estimated IC_{50} of 4 ± 0.7 nM for BOS-981, 32 ± 4 nM for BOS-857 and 35 ± 5 nM
228 for BOS-318. As well, BOS-inhibitors inhibited endogenous Furin-like processing of a dibasic
229 bone morphogenic protein 10 (BMP10)-mimic (43) with an IC_{50} of ~8 nM *versus* 5 nM for the
230 dec-RVKR-cmk as determined by a cell-based Golgi imaging assay with U2OS cells (Fig. 4D).
231 We further showed that BOS-inhibitors efficiently blocked S1/S2 and S2' processing by
232 endogenous Furin-like enzymes, resulting in a near complete inhibition at 0.3 μM, also obtained
233 with 50 μM of dec-RVKR-cmk (RVKR; Fig. 4E). Overall, our data clearly demonstrate a role of
234 Furin in the processing of proS at the S1/S2 and S2' sites.
235

Furin-like inhibitors reduce virus production in SARS-CoV-2-infected cells. We next examined whether blocking the processing of proS by BOS-inhibitors modulates SARS-CoV-2 infection. Indeed, in lung derived Calu-3 cells pretreated with 1 μM BOS-inhibitors for 24h before infection, we observed significantly decreased viral titers at 12, 24 and 48h post-infection (Fig. 5A). Importantly, the inhibitory effect was dose-dependent, reducing viral burden up to >30-fold with 1 μM BOS-318 (Fig. 5B; left panel). As well, the IC_{50} and selectivity index (44) of BOS-318 were 0.2 μM and 475, respectively (Fig. 5B; right panel). Importantly, the levels of spike (full length and cleaved S) and nucleocapsid proteins in the supernatant and cells were decreased in a dose-dependent manner (Fig. 5C), underscoring the crucial role played by Furin-like convertases in SARS-CoV-2 infection in this lung epithelial cell model. A similar analysis with BOS-857 and BOS-981 revealed comparable antiviral effects and selectivity index (SI-Figs. 3A, B). In addition, BOS-inhibitors were also evaluated in Vero E6 cells where SARS-CoV-2 entry and infection is established primarily *via* the endocytic pathway (11, 24). In this system and as expected, treatment with BOS-inhibitors led to weaker effect since we observed a decreased virus production by only ~2.6-5.7-fold (SI-Fig. 4), possibly reflecting a role of Furin-like activity in early endosomes (36) for pH-dependent virus entry in Vero cells.

Since TMPRSS2 has been proposed to be important for viral entry at the plasma membrane, we next determined whether combining BOS-inhibitors and the TMPRSS2-inhibitor Camostat would have a synergistic effect, leading to a more pronounced antiviral effect in Calu-3. As shown, although these compounds could reduce viral replication individually, their co-treatment resulted in a synergistic inhibition of ~95 ± 2.5% (>70-fold) of progeny infectious viruses (Fig. 5D and SI-Fig. 5), reinforcing the importance of both Furin-like proteases and TMPRSS2 in promoting efficient SARS-CoV-2 infection of Calu-3 cells.

Furin-like inhibitors reduce viral entry by blocking processing of proS during biosynthesis and at the viral entry site. The more dramatic impact observed with Furin-like inhibitors on virus infection of Calu-3 cells *versus* Vero cells suggests that these inhibitors affect mainly the pH-independent entry mechanism. Thus, we next assessed the effect of BOS-inhibitors on viral entry. Using nanoluciferase-expressing HIV particles pseudotyped with WT, μS1/S2 or μS2' S-proteins, we observed that the viral entry of μS1/S2-S pseudovirions is ~10-fold reduced in Calu-3 cells (Fig. 6A). In contrast, all three pseudotyped viruses were at least 10-fold more infectious in HEK293T-ACE2 cells, suggesting that S-priming at S1/S2 is required for optimal viral entry in Calu-3 cells, but dispensable or perhaps even less desirable in HEK293T-ACE2 cells (Fig. 6A). Since these findings were similar to those in Vero E6 cells (45), we surmise that viral entry in HEK293T-ACE2 cells was through the same pH-dependent, endocytic route as reported for Vero cells (46, 47). This agrees with the fact that HEK293 cells allow endocytosis of SARS-CoV-2 pseudovirions *via* clathrin-coated vesicles (48). In the case of μS2'-S-expressing viral particles, entry was more efficient in both cell types (compare the same-coloured dots between WT-S and μS2'-S in absence of BOS, Fig. 6A), implying that S cleavage at the S2'optimized Furin-like site could enhance viral entry. When BOS-318 was present during biosynthesis of pseudovirions, processing of WT-S and μS2'-S was blocked (Fig. 6B), leading to reduced viral entry in Calu-3 by ~3.6- to ~12.5-fold, respectively (Fig. 6A). Thus, BOS-318 treatment phenocopied the effect of the μS1/S2 in both cell types. Nevertheless, under this condition viral entry in HEK293T-ACE2 cells was enhanced by ~10-fold for WT-S and ~2-fold for μS2'-S (Fig. 6A), suggesting that viral entry by the pH-dependent pathway does not require FCS processing.

Having observed the negative effect of BOS-318 on S processing by particle-producing cells, we asked whether pre-treating target cells with BOS-318 would also affect entry of SARS-CoV-2 pseudoparticles. In Calu-3 cells, where viral entry occurs primarily through fusion at the plasma

283 membrane (46), we observed reduced viral entry by ~3.8-fold for WT-S and ~14-fold for μS2'-S (Fig.
284 6C). This emphasizes a significant contribution of Furin to the processing and priming of S at the
285 plasma membrane of Calu-3 cells after ACE2 recognition. The fact that BOS-318 had a more
286 pronounced effect on entry by μS2'-S-containing viral particles was not surprising given the very
287 efficient S2' processing of this mutant by Furin (Fig. 2D). Of note, viral entry by WT-S pseudoparticles
288 was more affected by 100 μM Camostat compared to that by μS2'-S viral particles (Fig. 6C). Here,
289 entry was reduced by ~8.6-fold for WT-S and ~3.2-fold for μS2'-S, suggesting that Furin plays a more
290 prominent role in the entry of μS2'-S *versus* WT-S viral particles. Lastly, the combined pre-treatment
291 of both BOS-318 and Camostat led to a complete block of viral entry, highlighting the importance of
292 both Furin and TMPRSS2 in mediating viral fusion at the plasma membrane.
293
294 **Furin-like inhibitors decrease cell-to-cell fusion and syncytia formation.** To assess whether
295 BOS-inhibitors also affect cell-to-cell fusion, we developed a co-culture assay in which donor HeLa
296 cells express HIV Tat and the fusogenic S-protein, while acceptor HeLa TZM-bl cells express ACE2
297 and Tat-driven luciferase (49) (Figs. 7A). As a proof-of-principle, we showed that when donor HeLa
298 cells expressing HIV gp160 and Tat fused with acceptor cells expressing CD4 (SI-Fig. 6A, panel b),
299 luciferase activity was increased compared to that observed in TZM-bl control cells co-cultured with
300 donor Hela cells expressing only Tat (SI-Fig. 6B). The expression of S-protein alone in donor HeLa
301 cells did not induce fusion with acceptor TZM-bl control cells (SI-Fig. 6B). However, ACE2
302 expression in TZM-bl allowed fusion with HeLa-expressing S-protein (SI-Fig. 6A, panel c; 6B) in a
303 dose-dependent manner (SI-Fig. 6C), but no fusion was observed with μS1/S2-S (SI-Fig. 6A, panel
304 d). Indeed, the linearity of our assay (correlation coefficient of 0.87) validated the use of luminescence
305 as an indicator of cell-to-cell fusion (SI-Fig. 6C). Using this assay, we found that while donor cells
306 expressing WT-S led to syncytia formation (Fig. 6B) and a >10-fold increased cell-to-cell fusion

compared to control (empty vector V, no S) cells (Fig. 6C), donor cells expressing μS1/S2-S did not promote any cell fusion even in the presence of ACE2 (Figs. 6C, D). Thus, the μS1/S2-S phenocopies the effect of BOS-inhibitors on cell-to-cell-fusion (Fig. 6C), whereby absence of Furin-activity would not allow fusion and demonstrates a key role of S1/S2 cleavage in S-mediated cell-to-cell fusion. Consistent with this finding, we observed an almost complete loss of cell fusion when donor cells were treated with BOS-inhibitors or the PC-inhibitor decanoyl-RVKR-cmk (RVKR; Fig. 6C) (43), emphasizing the critical role of Furin-cleavage in promoting ACE2-dependent cell-to-cell fusion in the context of acceptor cells that do not endogenously express TMPRSS2, such as HeLa cells. This fusion assay also enabled the assessment of the effects of some worldwide-spreading S-protein variants of SARS-CoV-2, which seem to affect viral traits such as transmissibility, pathogenicity, host range, and antigenicity of the virus (50, 51). Among these, we selected mutants that modify the Pro at the P5 position of the S1/S2 site (Fig. 1A), i.e., the P681H and P681R associated with the α- and δ- variants, respectively (9). Our data showed that while the μS2' mutant did not affect cell-to-cell fusion, the P681H and P681R mutants significantly enhanced it by ~2-fold (Fig. 7D), in line with the higher transmissibility of the associated α- and δ- SARS-CoV-2 variants (50, 51) and increased cell-to-cell fusion (52).

TMPRSS2 promotes cell-to-cell fusion in the absence of Furin-mediated cleavage at S1/S2. Having shown the critical role of Furin-cleavage in promoting ACE2-dependent cell-to-cell fusion in HeLa cells that do not express TMPRSS2, we next examined the importance of TMPRSS2 in cell-to-cell fusion given its significant role in viral entry and replication (Figs. 5D and 6C). Thus, we analyzed fusion between donor cells expressing WT-S or μS1/S2-S (double tagged S-protein: HA at the N-terminus and V5 at the C-terminus) and acceptor cells expressing ACE2 in the absence or the presence of TMPRSS2 (Fig. 8). As shown, in the presence of ACE2, TMPRSS2 reduced fusion by ~2.1-fold in

the case of WT-S but increased it by ~2.4-fold in the case of μS1/S2-S (Fig. 8A). Under the same conditions, WB analyses showed that for WT-S, the TMPRSS2 expression decreased by ~4-fold (3.8 *versus* 0.9) the relative levels of S2 and modestly increased by ~1.5-fold (0.6 *versus* 0.9) the relative levels of S2'. In contrast, for μS1/S2-S, expression of TMPRSS2 increased S2' levels by ~7-fold (0.1 *versus* 0.7) without any detectable change in S2 (0.6 *versus* 0.5) (Fig. 8B). Therefore, in the presence of ACE2, the levels of S2 correlate with cell-to-cell fusion in the case of WT-S that is well cleaved at S1/S2 by Furin. In contrast, fusion correlates best with S2' levels, when cleavage at S1/S2 is limited (μS1/S2-S). Interestingly, secretion of the HA-tagged, N-terminal S1 subunit (aa 14-685; Fig. 1A) was more pronounced for WT-S compared to μS1/S2-S (Fig. 8B). Yet, in both cases, the extent of S1 release was not modulated by the presence of TMPRSS2, suggesting that TMPRSS2-mediated enhanced fusion of μS1/S2 was not a consequence of altered S1/S2 cleavage (Fig. 8B).

Mechanism by which TMPRSS2 promotes cell-to-cell fusion. To assess whether TMPRSS2 promoted cell-to-cell fusion by enhancing S2' cleavage in the complete absence of S1/S2 priming, we generated a new S-derivative lacking all Arg at S1/S2 (Fig. 1), namely μAS1/S2 ($AAAA_{685}$)-S, and hence different from μS1/S2 (Fig. 1C; ARAA mutant), it would not be cleaved by TMPRSS2 or Furin. Cell-to cell fusion was assessed following incubation of cells expressing WT-S or μAS1/S2-S with acceptor cells expressing ACE2 and/or TMPRSS2. In this context, TMPRSS2 reduced fusion of WT-S by ~2.6-fold and enhanced that of μAS1/S2-S by ~3.1-fold (Fig. 9A), as previously observed with the μS1/S2 mutant (Fig. 8A). Camostat completely restored TMPRSS2-reduced fusion with WT-S and largely attenuated the TMPRSS2-enhanced fusion with μAS1/S2 (Fig. 9A). This revealed that in the presence of ACE2, TMPRSS2 could enhance fusion in absence of S1/S2 priming. We next assessed whether this effect could be related to the differential processing of the S protein and/or to ACE2

receptor shedding by TMPRSS2. The WB of cell lysates shows that treatment of acceptor cells with Camostat eliminated the TMPRSS2-induced reduction in S2 observed with WT-S (Fig. 9B), yet it did not significantly alter S2' levels either with WT-S or μAS1/S2 (Figs. 9B, C). In contrast, the WB of ACE2 reveal that TMPRSS2 strongly reduced the levels of mature membrane-bound ACE2 migrating at ~120 KDa, without affecting the lower molecular weight protein which correspond to an immature ER-retained form of ACE2 ($ACE2_{im}$, Figs. 9B, C) that is sensitive to endoH digestion (*not shown*). These results show that ACE2 is shed by TMPRSS2, as proposed in earlier studies (33). As expected, we observed that ACE2 shedding by TMPRSS2 is almost completely blocked by Camostat (compare ACE2+TMP lanes DMSO to CAM) (Figs. 9B and C).

In contrast, the WB anti ACE2 reveal that TMPRSS2 strongly reduced the levels of mature membrane-bound ACE2 migrating at ~120 KDa, without affecting the lower molecular weight protein which correspond to an immature ER-retained form of ACE2 ($ACE2_{im}$, Figs. 9B, C) that is sensitive to endoH digestion (*not shown*). These results suggest that ACE2 is shed due to TMPRSS2 cleavage as proposed in earlier studies (33). As expected, we observed that this effect of TMPRSS2 on ACE2 processing is almost completely blocked by Camostat (compare ACE2+TMP lanes DMSO to CAM) (Figs. 9B and C). Finally, by analysing the release of S1 in the cell culture media we observed that TMPRSS2-induced release into the media of a longer ~175 kDa fragment from μAS1/S2, referred hereafter as $S1_L$ (Fig. 9C), which is not detected in presence of Camostat. The molecular weight of the $S1_L$ indicates that it corresponds to a TMPRSS2 cleavage of μAS1/S2-S at S2' (Fig. 9B).

These results suggest that TMPRSS2 modulation of fusion is complex, as TMPRSS2 alters both the integrity of ACE2 receptor, but also participates in S-processing as attested by the release of $S1_L$ which corresponds to the N-terminal cleavage product of μAS1/S2-S at S2'. Interestingly, we did not detect an associated increase in S2' levels, suggesting that after cleavage the fusion process occurs and the S2 protein is subsequently degraded, as suggested by a small degradation product seen on WB

(arrow in Figs. 9B, C). We surmise that in the presence of ACE2, TMPRSS2 facilitates the secretion of the N-terminal fragment $S1_L$ generated by cleavage at S2'.

Our next goal was to further decipher the contribution of ACE2 cleavage by TMPRSS2 and the seemingly opposite effects of TMPRSS2 on fusion activity with WT-S and μAS1/S2-S (and μS1/S2-S). Hence, since TMPRSS2 cleaves at single Arg and Lys residues (53), we tested the effect of multiple Arg/Lys to Ala mutants in segments close to the transmembrane domain of ACE2 (C0 + C4 in Fig. 10A), which were previously proposed to limit the TMPRSS2-induced shedding (54). Accordingly, WB analyses (Fig. 10B) revealed that TMPRSS2, but not its Ser* active site S441A mutant (μTMPR, Fig. 10B; SI-Fig. 7) sheds the membrane-bound ~120 kDa WT ACE2, releasing a major ~95 kDa and a minor ~80 kDa form into the media. In contrast, TMPRSS2 primarily generated the ~80 kDa fragment from the ACE2 (C0+C4) mutant. It should be mentioned that in the absence of TMPRSS2 the extent of fusion for both WT-S and μAS1/S2-S was comparable between ACE2 (WT) and ACE2 (C0+C4). Interestingly, in the context of the ACE2 (C0+C4) receptor mutant, we found that TMPRSS2 no longer modulates the fusion of both WT-S and μAS1/S2-S (Fig. 10C). Importantly, and different from WT ACE2 (Figs. 8, 9), TMPRSS2 did not reduce the levels of S2 when ACE2 (C0+C4) was used (Fig. 10D), nor did it reduce fusion (Fig. 10C). Additionally, the TMPRSS2-enhanced secretion of the ~ 175 kDa $S1_L$ fragment in the absence of S1/S2 cleavage (Fig. 9C; SI-Fig. 7), was no longer detected in the media when ACE2 (C0+C4) was expressed on acceptor cells (Fig. 10D), correlating with the lack of fusion of μAS1/S2-S (Fig. 10C). Altogether, these results suggest for the first time that in the absence of Furin-mediated priming of S, TMPRSS2 promotes cell-to-cell fusion by generating a ~95 kDa sACE2 that likely binds the $S1_L$ cap (55) and favors its release.

DISCUSSION

Furin and TMPRSS2 have both been proposed to process the SARS-CoV-2 spike protein and promote viral entry and infection. In this study, we functionally characterize the role of Furin and TMPRSS2 and show their complementary role in SARS-CoV-2 mechanism of entry and infection.

Consistent with previous data (18, 33, 56, 57), processing at S1/S2 is required for optimal viral entry in Calu-3 lung epithelial cells. Indeed, mutation of the arginines of the FCS or blocking S1/S2 cleavage by a series of novel Furin-inhibitors effectively reduced SARS-CoV-2 entry in Calu-3 cells. In the context of cell-to-cell fusion, mutations of the FCS impaired syncytia formation in HeLa cells in the absence of TMPRSS2 in acceptor cells, and Furin-inhibitors phenocopied the effect of these S1/S2 mutations. These results highlight the importance of Furin in promoting S-mediated cell-to-cell fusion. In contrast, in HEK293T cells, where SARS-CoV-2 likely enters *via* endocytosis in acidic endosomes, mutations of the FCS enhanced entry (Fig. 6), suggesting that cleavage at S1/S2 by Furin was not required for efficient S-processing by endosomal proteases (e.g., cathepsins) (58, 59). The pH-dependent entry pathway is sensitive to drugs increasing the pH of endosomal compartments, e.g., hydroxy-chloroquine (47). Nevertheless, this drug failed to show significant improvement in COVID-19 patients (60, 61) or infected animals (62), supporting the notion that the virus can effectively utilize alternative entry pathways that are critical for virus entry, transmission and pathogenicity. The fact that Furin-cleavage at S1/S2 is conserved in SARS-CoV-2 isolated from COVID-19 patients and that ΔPRRA viruses are poorly infectious in hamsters (60), suggest that blocking viral entry through the pH-independent pathway is a viable approach towards thwarting SARS-CoV-2 dissemination. In this context, the non-toxic, small molecules BOS-inhibitors that were analyzed in this study, which can be delivered orally or by inhalation, deserve consideration as potential antivirals against acute SARS-CoV-2 infection. As observed in adult animal models, short-term inhibition of Furin would not cause severe side effects, despite the many physiological functions of this enzyme (20).

Our results also demonstrate that Furin can also process S at S2', a site that we map by proteomics to be at **KR**$_{815}$↓SF. The latter S2' cleavage site was confirmed by introducing an optimized S2' site (μS2', KRRKR$_{815}$↓SF) that was efficiently cleaved by Furin, yielding a protein fully competent for fusion in pseudotyped experiments. Importantly, we showed that the S2' processing is strongly increased when ACE2 receptor is expressed. Our results suggest that the recognition of the ACE2 receptor by the spîke protein induces a conformational change of the S2 domain and enhances cleavage of S2' site by cellular proteases such as Furin.

In contrast TMPRSS2 appears to cleave synthetic peptides encompassing the S1/S2 and S2' cleavage sites and proS protein in Hela cells less efficiently compared to Furin. TMPRSS2 has been reported to enhance the infectivity of SARS-CoV-1 and MERS-CoV *via* cleavages of the S-protein (53, 63), as reviewed in (4, 15, 23). The S1/S2 site VSLL**R**$_{667}$↓ST of SARS-CoV-1 contains an Arg↓Ser cleavage motif that is propitious to cleavage by TMPRSS2 (53) but not by Furin. However, S1 production was minimal and fusion was observed only when donor cells expressing S-protein were co-cultured with acceptor cells expressing ACE2 and TMPRSS2 (53). In SARS-CoV-2 the S1 released, presumably following cleavage of S at S1/S2 and ACE2 binding, is much reduced with μS1/S2-S compared to WT-S, indicating that Furin-mediated cleavage at S1/S2 promotes a more efficient release of S1 (Fig. 8B). Additionally, in a co-culture system the relative levels of soluble S1 fragment were not affected by the presence or absence of TMPRSS2 for WT and μS1/S2 (Fig. 8B). This suggests that the differential effect of TMPRSS2 on cell-to-cell fusion could not be attributed to its direct cleavage activity on S. Rather, we assert that TMPRSS2 primarily modulates cell-to-cell fusion in part *via* shedding of ACE2. In the presence of TMPRSS2 the extent of fusion would depend on a combination of reduced levels of full-length cell surface ACE2 and increased levels of sACE2 that could act as a decoy to inhibit fusion (64). In that context, a human recombinant sACE2 that includes the collectrin domain but lacks the TM domain (hrsACE2, aa 1-740) (see Fig. 10A) effectively

blocked SARS-CoV-2 infection of Vero E6 cells (55). Indeed, our cell-to-cell fusion assay tested in co-culture revealed that the ~95 kDa sACE2 primarily produced by TMPRSS2 cleavage of ACE2 resulted in lower levels of cellular ACE2 (Figs. 9B, 10B) and in impaired WT-S induced fusion (Figs. 9A, 10C). In contrast, the mutant ACE2 (C0+ C4) was no longer sensitive to TMPRSS2 impairment of WT-S-induced fusion, suggesting that the ~80 kDa form of sACE2 primarily produced by TMPRSS2 cleavage of ACE2 (C0+C4), likely upstream of Lys_{619}, may no longer be able to inhibit WT-S-fusion (Fig. 10C), but may still bind S1 as shown by cryoEM studies that used a short ACE2 ectodomain (aa 19-615) (40). Altogether, these results suggest that the C-terminal collectrin-like domain (65, 66) of ACE2 (aa 616-768) (Fig. 10A), which is lost in the ~80 kDa form, may be critical for the ability sACE2 to inhibit cell-to-cell fusion of WT-S. Since Arg_{710} and Arg_{716} within the collectrin-like domain (Fig. 10A) have been reported to be implicated in ACE2 dimerization (66), their Ala mutation in the ACE2 (C0+C4) mutant should significantly impair ACE2 dimerization. Whether dimerization of ACE2 and the ~95 kDa sACE2 (Fig. 10B) are needed for efficient inhibition of WT-S-induced fusion (64) is yet to be confirmed.

In the context of endogenous expression of ACE2 and TMPRSS2, e.g., in Calu-3 cells (67, 68), our data show that Camostat significantly reduces SARS-CoV-2 infectivity (Fig. 6C), revealing that a TMPRSS2-like activity favors viral entry. Similarly, in the presence of BOS-inhibitors or absence of Furin cleavage at S1/S2, TMPRSS2 enhances cell-to-cell-fusion (Figs. 8A, 9A). HeLa cells expressing WT-S in donor cells and both ACE2 and TMPRSS2 in acceptor cells, exhibited reduced cell-to-cell fusion, a process inhibited by Camostat. This suggests that the relative contribution of TMPRSS2 to the shedding of ACE2 into sACE2 and cleavage of S-protein at S2' is cell-type dependent. Future experiments may unravel the underlying mechanism that would explain the difference between the HeLa and Calu-3 cells. Our study highlights a complex dynamic between spike, ACE2, Furin and TMPRSS2 (Fig. 11) and points to a potential role of TMPRSS2, which in the absence of S1/S2

474 processing (e.g., μAS1/S2 or in presence of BOS-inhibitors) can by shedding ACE2 facilitate S2'
475 cleavage and cell-to-cell fusion.

476 The human airway epithelium is an important site of early SARS-CoV-2 infection (18, 24, 69). The
477 virus can then disseminate to other tissues/cells such as gut, liver, endothelial cells and macrophages
478 where ACE2, Furin and TMPRSS2 are co-expressed (70). While Furin is mostly found in the TGN, it
479 is also present in endosomes and on apical/basolateral plasma membranes in polarized cells such as
480 those of the lung, small intestine and kidney (71). In contrast, TMPRSS2 is mostly found at the apical
481 membrane of secretory epithelia (72), suggesting that both enzymes would be poised to process the S-
482 protein on the apical side. Their relative abundance may be an important factor governing which of the
483 two might cleave S at the S2' cleavage site. The complementarity and interchangeability of these
484 different proteases, together with those in endosomes, likely allows SARS-CoV-2 to exhibit a wider
485 tropism compared to SARS-CoV-1 (73). In this context, we note that randomized placebo controlled
486 clinical trials using an orally administered TMPRSS2 inhibitor Camostat mesilate three times a day for
487 treatment of COVID-19 patients did not show improvement in outcomes (74). We believe that the
488 maximal benefit of TMPRSS2 inhibition could be achieved when Furin activity is also inhibited, since
489 our results showed that TMPRSS2 activity is preponderant in the context of absence of cleavage at
490 S1/S2. Furthermore, the intranasal delivery of both agents would be expected to have less side effects
491 and be more effective, as it would directly target the airway epithelia of the nose and the lungs, the
492 major sites of SARS-CoV-2 entry.

493 Altogether, our results strongly support the notion that a combination of BOS- and selective
494 TMPRSS2-inhibitors would provide a more effective blockade against SARS-CoV-2 infection
495 (Figs. 5D, 11). It would now be interesting to validate *in vivo* whether a combination of a BOS-
496 inhibitor and a more potent/selective TMPRSS2-inhibitor (75) together with hydroxy-chloroquine
497 (56, 76) would synergize the antiviral effect of these entry inhibitors.

The availability for worldwide distribution of various SARS-CoV-2 vaccines that inhibit the accessibility of the RBD of S-protein to ACE2 (https://www.raps.org/news-and-articles/news-articles/2020/3/covid-19-vaccine-tracker) represents a major advance to limit the spread of SARS-CoV-2 infections. However, it is still not known with certainty whether they will be effective in patients with impaired immune systems, and whether they will confer a persistent protection against new variants of SARS-CoV-2. If the protective effect of the vaccination remains incomplete, effective antiviral drugs are still needed and could help with early diagnosis of the disease. Ultimately, in case of new emerging coronavirus pandemics (77), the availability of such treatments would constitute a powerful anti-viral arsenal to be used in pandemic preparedness.

MATERIALS AND METHODS

Enzymatic PC-inhibition by BOS-inhibitors

Biochemical assay: The proprotein convertases Furin (108-574-Tev-Flag-6His), PC5A (PCSK5; 115-63-Tev-Flag-6His), PACE4 (PCSK6; 150-693-Tev-Flag-6His), and PC7 (PCSK7; 142-634-Tev-Flag-6His) enzymes were purified from BacMam transduced CHO cells. Reactions were performed in black 384-well polystyrene low volume plates (Greiner) at a final volume of 10 µL. BOS-inhibitors (BOS-318, BOS-857 and BOS-981) were dissolved in DMSO (1 mM) and serially diluted 1 to 3 with DMSO through eleven dilutions to provide a final compound concentration range from 0.00017 to 10 µM. 0.05 µl of each concentration was transferred to the corresponding well of an assay plate, and then 5 µl of enzyme (Furin, PCSK5, PCSK6, and PCSK7) in assay buffer (100 mM HEPES pH7.5, 1 mM $CaCl_2$ and 0.005% Triton X-100) was added using a Multidrop Combi (Thermo) to the compound plates to give a final protein concentration of 0.02, 0.5, 2.5, and 1.0 nM respectively. The plates were mixed by inversion and following a 30 min preincubation of enzyme with compound at room temperature (~22ºC), the substrate FAM-QRVRRAVGIDK-TAMRA (AnaSpec # 808143, 5 µl of a 1, 0.25, 0.20, and 0.5 µM solution in assay buffer for Furin, PCSK5, PCSK6, and PCSK7 respectively) was added using a Multidrop Combi. The plates were centrifuged at 500 x *g* for 1 minute and incubated at room temperature for two hours. Enzyme inhibition was then quantified using an Envision instrument (PerkinElmer). Data were normalized to maximal inhibition determined by 1 µM decanoyl-Arg-Val-Lys-Arg-chloromethylketone (Calbiochem #344930).

Golgi imaging assay: This assay uses an image-based platform to evaluate the intracellular activity of Furin inhibitors. Reactions were performed in black 384-well, tissue culture-treated, clear bottom plates (Greiner). Compounds dissolved in DMSO (1.0 mM) were serially three-fold diluted

to give a final compound concentration range from 0.00017 to 10 μM. Analyses were initiated by the addition of U2OS cells simultaneously transduced with a BacMam-delivered construct containing a Golgi-targeting sequence followed by a 12-amino acid Furin/PCSK cleavage site from Bone Morphogenic Protein 10 (BMP10) and then GFP at the C terminus. The dibasic Furin cleavage site sequence was flanked by glycine rich linkers (GalNAc-T2-GGGGS-DSTARIRRNAKG-GGGGS-GFP). Briefly, frozen cells are thawed in assay media (Dulbecco's Modified Eagles Medium Nutritional Mixture F-12 (Ham) without phenol red containing 5% FBS) and diluted to deliver 6000 cells/well (50 μl) to the plate using a Multidrop Combi (Thermo). After a 24-hour incubation period at 37ºC, the cells are stained with Cell Mask Deep Red, fixed in paraformaldehyde and the nuclei stained using Ho33342. The Golgi-targeted GFP forms bright punctate clusters within the cell. In the absence of a Furin/PCSK inhibitor, the endogenous protease cleaves GFP from its N-acetylgalactosaminyltransferase-2 Golgi tether, releasing GFP into the Golgi lumen where fluorescence was diluted below the threshold of assay sensitivity. In the presence of a cell permeable Furin/PCSK inhibitor, GFP fluorescence increases as intra-Golgi protease activity was reduced. Cellular GFP intensity was determined by image-based acquisition (Incell 2200, Perkin Elmer) at 40x magnification with 4 fields measured per well. Multi-scale top hat segmentation was used to identify the GFP-tagged puncta and to quantitate the average fluorescence of all puncta on a per cell basis. Cellular toxicity was determined in parallel.

Furin and TMPRSS2 fluorogenic assays: Recombinant Furin was purchased from BioLegend (#719406), human recombinant TRMPSS2 from Cliniscience (ref LS-G57269-100), and the DABCYLGlu-EDANS labelled peptides encompassing the different cleavage sites (SI Table 1) were purchased from Genscript. Reactions were performed at room temperature in black 384-well polystyrene low volume plates (CELLSTAR-Greiner Bio-One # 784476) at a final volume of 15

554 µL. The fluorescent peptides were used at 5 µM and the reactions were performed in 50 mM Tris
555 buffer (pH 6.5 or 7.5), 0.2% Triton X-100, 1mM $CaCl_2$ and Furin was added at a final
556 concentration of 0.2 to 100 nM. BOS-inhibitors (BOS-318, BOS-857 and BOS-981) were
557 dissolved in DMSO (1 mM) and serially diluted 1 to 2 with DMSO to provide a final compound
558 concentration range from 50 µM to 0.01 nM with 5% DMSO in the enzymatic assay. For
559 TMPRSS2, the fluorescent peptides were used at 5 µM and the reactions were performed in 50
560 mM Tris buffer (pH 8), 150 mM NaCl and TMPRSS2 was added at final concentrations of 50 nM.
561 Cleavage of the synthetic peptides was quantitated by determining the increase of EDANS (493
562 nM) fluorescence following release of the DABCYL quencher, which was excited at 335 nM using
563 a Safire 2 Tecan fluorimeter. The fluorescence was followed during 90 min, and the enzymatic
564 activity was deduced by measurement of the increase of fluorescence during the linear phase of
565 the reaction. Each reaction was performed in triplicate and the standard deviation was calculated
566 using Excel-ecart type function ($\sqrt{\frac{\sum(x-\bar{x})^2}{(n-1)}}$).

567 **Plasmids**

568 Single tagged (C-terminal V5 tag) or double tagged (N-terminal HA tag and C-terminal V5 tag)
569 spike-glycoprotein of SARS-CoV-2 (optimized sequence) and its mutants were cloned into the
570 pIRES2-EGFP vector. Site-directed mutagenesis was achieved using a Quick-Change kit
571 (Stratagene, CA) according to the manufacturer's instructions. The plasmids pCI-NEO-hACE2
572 received from DW Lambert (University of Leeds) and pIRES-NEO3-hTMPRSS2 from P Jolicoeur
573 (IRCM). The ΔEnv Vpr Luciferase Reporter Vector (pNL4-3.Luc.R-E-) was obtained from Dr.
574 Nathaniel Landau through the NIH AIDS Reagent Program whereas the pHIV-1NL4-3 ΔEnv-
575 NanoLuc construct was a kind gift from Dr. P Bieniasz. Plasmids encoding VSV-G, as HIV-1
576 Env and tat were previously described (78, 79).

577 **Cell culture and transfection**

578 Monolayers of HeLa, HEK293T, HEK293T17, Vero E6 and Calu-3 cells were cultured in 5% CO_2
579 at 37°C in Dulbecco's modified Eagle's medium (DMEM; Wisent) supplemented with 10% (v/v)
580 fetal bovine serum (FBS; Wisent). HEK293T-ACE2(80), a generous gift from Dr. Paul Bieniasz,
581 were maintained in DMEM containing 10% FBS, 1% nonessential amino acids (NEAA) and 50
582 µg/ml blasticidin (Invivogen). The cells were transfected with JetPrime transfection reagent
583 according to the manufacturer's instructions (Polyplus transfection, New York, USA). At 24h post
584 transfection, the culture media were changed to serum-free and cells incubated for an additional
585 24h. To establish the HeLa cells stably express human ACE2, transfected cells were selected using
586 media containing 500 µg/ml of neomycin (G418, Wisent).

587 For knockdown of Furin in HeLa cells, an optimized set of 4 small interfering RNAs (siRNAs;
588 SMARTPool) targeted against human Furin were purchased from Horizon Discoveries (Perkin
589 Elmer, Lafayette, LA, USA) and transfections of HeLa cells were carried out using INTERFERin
590 (PolyPlus) as recommended by the manufacturer.

591 To generate HIV particles pseudotyped with SARS-CoV-2 S, 293T17 cells (600,000 cells plated
592 in a 6-well vessel) were transfected with 1 µg pNL4-3 Luc.R-E- (or pHIV-1NLΔEnv-NanoLuc)
593 in the presence or absence of 0.3 µg pIR-2019-nCoV-S V5 plasmids using Lipofectamine-3000
594 (Life Technologies). In certain experiments, 293T17 cells were treated with BOS-inhibitors at 6 h
595 post transfection. Pseudovirions expressing the nano- or firefly-luciferase were collected at 24 h
596 or 48 h post transfection, respectively. Viral supernatants were clarified by centrifugation at 300 x
597 *g,* passed through a 0.45-µm pore-size polyvinylidene fluoride (PVDF; Millipore) syringe filter
598 (Millipore; SLGVR33RS), and aliquots frozen at −80°C. For WB analysis of purified
599 pseudovirions, viral supernatants were concentrated by ultracentrifugation on a 20% sucrose

cushion for 3h at 35,000 RPM; Beckman Coulter OPTIMA XE; Ti70.1 rotor). HIV particles lacking the SARS-CoV-2 S glycoprotein served as a negative control in all experiments.

Cell viability assay using MTT

Cells, seeded in a 96-well plate, the day before, at 10,000 (HEK-293T and Vero E6) or 50,000 (Calu-3) cells, were treated with serial 10-fold dilutions of BOS-inhibitors for up to 48h. Cells treated with vehicle alone were used as negative control. MTT was subsequently added to the medium (final concentration: 2.5 mg/ml) and cells were further incubated for 4h at 37 ^{0}C. After removal of the culture media, DMSO was added and absorbance read at 595 nm using a microplate spectrophotometer. The data from two independent experiments done in triplicates was used to calculate the CC50 by nonlinear regression using GraphPad Prism V5.0 software.

Western blots

The cells were washed with PBS and then lysed using RIPA buffer (1% Triton X-100, 150 mM NaCl, 5 mM EDTA, and 50 mM Tris, pH 7.5) for 30 min at 4ºC. The cell lysates were collected after centrifugation at 14,000 × g for 10 min. The proteins were separated on 7% tris-glycine or 8% tricine gels by SDS-PAGE and transferred to a PVDF membrane (Perkin Elmer). The proteins were revealed using a V5-monoclonal antibody (V5-mAb V2660; 1:5000; Invitrogen), ACE2 antibody (rabbit monoclonal ab108252; 1:3,000; Abcam), Actin antibody (rabbit polyclonal A2066; 1:5,000; Sigma), or HA-HRP antibody (12-013-819; 1:3,500; Roche). The antigen-antibody complexes were visualized using appropriate HRP conjugated secondary antibodies and enhanced chemiluminescence kit (ECL; Amersham or Bio-Rad) and normalization was reported to β-actin. Quantification of immune-bands was performed using Image Lab software (Bio-Rad).

For analysis of SARS-CoV-2 S virions or pseudovirions, protein extracts of purified viral particles and corresponding producing cells (Calu-3 or 293T17, respectively) were resolved on

623 10% tris-glycine gels and immunoblotted for spike, nucleocapsid, HIV-1 Gag p24 or actin using
624 anti-V5 (for pseudovirion detection; V2660)/anti-S2 (for virion detection; Sino Biologicals;
625 40590-T62), anti-N (Sino Biologicals; 40143-MM05), anti-p24 (MBS Hybridoma line 31-90-25)
626 or anti-actin (MP Biomedicals, SKU 08691001), respectively.

627 **Glycosidase treatment**

628 30 to 50 µg proteins were digested for 90 min at 37ºC with endoglycosidase-H (Endo-H; P0702L)
629 or endoglycosidase-F (Endo-F; P0705S) as recommended by the manufacturer (New England
630 Biolabs).

631 **Inhibitor treatment**

632 At 24h post transfection, cells were incubated for 6h with two pan-PC inhibitors: the cell permeable
633 decanoyl-RVKR-chloromethylketone (cmk; 50 mM; 4026850.001; Bachem) or with the cell
634 surface PC-inhibitor hexa-D-arginine (D6R; 20 µM; 344931; EMD). Culture media were then
635 replaced with fresh ones containing the inhibitors for an additional 24h. For the selective cell-
636 permeable Furin-like inhibitors (BOS; Boston Pharmaceuticals), the cells were treated with the
637 inhibitors at the specified concentration starting at 5h pre-transfection and throughout the duration
638 of the experiment.

639 **Cell-to-cell fusion assay**

640 HeLa or HeLa TZM-bl cells were plated at 200,000 cells in 12-well plates. HeLa cells were
641 transiently transfected with different constructs of SARS-CoV-2 spike or NL4.3-HIV Env, or an
642 empty vector and 0.2 µg of CMV-Tat plasmid. HeLa TZM-bl cells were transfected with human
643 ACE2, TMPRSS2 or a combination of both. At 6h post-transfection, media were replaced with
644 fresh ones containing Furin-inhibitors, and 24h later the cells were detached with PBS-EDTA (1
645 µM). Different combinations of HeLa and HeLa-TZM-bl cells were placed in co-culture plate at a

ratio of 1:1 for a total of 60,000 cells/well of a 96 well place. After 18-24h the media were removed and 50 µl of cell lysis reagent was added in each well. 20 µl of the cell lysate was used for luciferase reading using 50 µl of Renilla luciferase reagent (Promega, Madison, WI, USA). Relative light units (RLU) were measured using a Promega GLOMAX plate reader (Promega, Madison, WI, USA) and values were reported as fold increase over the RLU measured in co-culture of HeLa cells transfected an empty vector (V) with respective TZM-bl cells.

Protein immunoprecipitation from co-culture media

When indicated, a secreted form of double tagged spike-glycoprotein of SARS-CoV-2 (N-terminal HA tag and C-terminal V5 tag) from media of co-cultured HeLa and HeLa-TZM-bl cells was analyzed by immunoprecipitation. Namely, 0.3 ml of media were precipitated with 25 µl EZ view Red anti-HA affinity gel (E 6779; Sigma-Aldrich) according to the manufacturers' protocol. Upon SDS-PAGE separation and PVDF transfer, the proteins were detected using an HA-HRP antibody (12-013-819; 1:3,500; Roche).

Microscopy

In our luciferase assay, cell co-cultures were plated on glass coverslips. After 18-24h, the cells were incubated with 488 CellMask™ to stain the membrane and then fixed with 4% PFA for 15 min at 4ºC. The glass coverslips were mounted on glass slides using ProLong™ Gold Antifade containing DAPI (Invitrogen). The number of syncytia were counted over 10 fields.

Immunofluorescence

Cell culture and transfection were performed on glass coverslips. Cells were washed twice with PBS and fixed with fresh 4% paraformaldehyde for 10 min at room temperature. Following washes, cells were either non-permeabilized or permeabilized with 0.2% Triton X-100 in PBS containing 2% BSA for 5 min, washed, and then blocking was performed with PBS containing 2%

669 BSA for 1h. Cells were incubated with primary antibodies overnight at 4°C using an antibody
670 against V5 (mouse monoclonal R960-25; 1:1000; Invitrogen), spike (mouse monoclonal
671 GTX632604; 1:500; GeneTex) and ACE2 (goat polyclonal AF933; 1:500; R&D Systems).
672 Following wash, corresponding species-specific Alexa-Fluor (488 or 555)-tagged antibodies
673 (Molecular Probes) were incubated for 1h at room temperature. Coverslips were mounted on a
674 glass slide using ProLong Gold Reagent with DAPI (P36935, Life Technologies). Samples were
675 visualized using a confocal laser-scanning microscope (LSM710, Carl Zeiss) with Plan-
676 Apochromat 63x/1.40 Oil DIC M27 objective on ZEN software.

677 **Pseudovirus entry**

678 HEK293T-ACE2 or Calu-3 (10,000 cells/well plated in a 96-well dish 24 or 48h before,
679 respectively) were incubated with up to 200 µl filtered pseudovirions for overnight. In certain
680 experiments, target cells were pretreated with BOS-318 (1 µM) for 6h and/or Camostat (40 µM)
681 for 2h before transduction. The overnight incubation with pseudovirions was performed in the
682 presence of the inhibitors. Viral inoculum was removed, then fresh media were added, and the
683 cells cultured for up to 72h. Upon removal of spent media, 293T-ACE2 and Calu-3 cells were
684 gently washed twice with PBS and analyzed for firefly- or nano- luciferase activity, respectively
685 using Promega luciferase assay (Cat # E1501) or Nano-Glo luciferase system (Cat # N1110),
686 respectively.

687 **Replication competent SARS-CoV-2 Viruses**

688 SARS-CoV-2, which served as the viral source, was originally isolated from a COVID-19 patient
689 in Quebec, Canada and was designated as LSPQ1. The clinical isolate was amplified, tittered in
690 Vero E6 using a plaque assay as detailed below, and the integrity of the S-protein multi-basic
691 protein convertase site validated by sequencing. All experiments involving infectious SARS-CoV-

692 2 virus were performed in the designated areas of the Biosafety level 3 laboratory (IRCM)
693 previously approved for SARS-CoV-2 work.

694 **Plaque assay in Vero E6 cells**

695 Vero E6 cells (1.2 x 10^5 cells/well) were seeded in quadruplicate in 24-well tissue culture plates in
696 DMEM supplemented with 10% FBS two days before infection. Cells were infected with up to six
697 ten-fold serial dilutions (10^{-2}-10^{-6}) of viral supernatant containing SARS-CoV-2 for 1h at 37ºC
698 (200 µl infection volume). The plates were manually rocked every 15 min during the 1-hour period.
699 Subsequently, virus was removed, cells were washed and overlaying media (containing 0.6% low
700 melt agarose in DMEM with 10% FBS) was added and incubated undisturbed for 60-65h at 37ºC.
701 Post incubation, cells were fixed with 4% formaldehyde and stained with 0.25% crystal violet
702 (prepared in 30% methanol). High quality plaque pictures were taken using a high resolution
703 DLSR camera (Nikon model: D80, objective: "AF Micro-Nikkor 60mm f/2.8D"). Plaques were
704 counted manually and in parallel, imaged plaque plates were processed and plaques enumerated
705 using an automated algorithm based Matlab software. Virus titer is expressed as plaque-forming
706 units per ml (PFU/ml): (number of plaques x dilution factor of the virus) x 1000 / volume of virus
707 dilution used for infection (in µl). Multiplicity of infection (MOI) expressed as: MOI = PFU of
708 virus used for infection / number of cells.

709 **Cell infections with fully replicative SARS-CoV-2**

710 Vero E.6 and Calu-3 cells were seeded in duplicates in 12-well plates (2.3 x 10^5 cells/well) the day
711 before. Cells were pre-treated with various concentrations (0.1-1µM) of BOS-inhibitors and
712 vehicle alone (DMSO) for up to 24h. In certain experiments, Calu-3 were also pre-treated with
713 Camostat for 1h. Thereafter, the cells were infected with SARS-CoV-2 virus at MOI of 0.001 for
714 1h (Vero E6) or 0.01 for 3h (Calu-3 cells) in 350 µl of serum-free DMEM at 37ºC with occasional

manual rocking of plates. Cells plus media only were used as a control. After incubation, virus was removed, and the cell monolayer was washed twice successively with PBS and serum-free DMEM. New media (total 1ml) containing the concentrations of BOS-inhibitors was subsequently added to cells. Cell-free supernatant (250 µl) was removed at 12, 24 and 48h post infection. The drugs were replenished for 1 ml media at 24h post-infection. The virus supernatants were stored at -80°C until further use. Viral production in the supernatant was quantified using a plaque assay on Vero E6.1 cells as described above. In certain experiments, viral supernatants were harvested at the end of infection and purified on a 20% sucrose cushion using ultracentrifugation as described above. The resulting concentrated virus and corresponding infected cells were analyzed by Western blotting as appropriate.

Quantification and statistical analysis: Virus titers quantified by plaque assay in triplicate were shown as mean ± standard deviation. The results from experiments done with two biological replicates and two technical replicates in triplicates were used to calculate the IC_{50} by nonlinear regression using GraphPad Prism V5.0 software. The difference between the control cells (virus with 0.001% DMSO) and the cells treated with BOS-inhibitors were evaluated by Student's t test. The P values of 0.05 or lower were considered statistically significant (*, $p < 0.05$; **, $p < 0.01$; ***, $p < 0.001$).

DATA AVAILABILITY

Source data are provided with this paper. The data that support the findings of this study are preserved at repositories of the Montreal Clinical Research Institute (IRCM), Montreal, QC, Canada and available from the corresponding authors upon reasonable request.

ACKNOWLEDGEMENTS

This work was supported in part by CIHR Foundation grants (NGS: # 148363) and (ÉAC: # 154324), a Canada Research Chairs in Precursor Proteolysis (NGS: # 950-231335), a CIHR CHAMPS Team Grant # HAL 157986 (NGS and ÉAC), Réseau SIDA maladies infectieuses COVID-19 initiative (ÉAC and NGS), the European score project and ANR Reacting COVID-19 (ED and BC). The authors thank the Quebec public health laboratory for providing the infectious isolate LSPQ1 SARS-CoV-2. We thank Paul Bieniasz for the 293T-ACE2 cell line and the pHIV-1NL4-3ΔEnv-NanoLuc construct. The following reagents were obtained from the NIH AIDS Reagent Program, Division of AIDS, NIAID, NIH: TZM-bl cells, from John C. Kappes, Xiaoyun Wu, and Tranzyme, Inc. and HIV-1 pNL4-3 ΔEnv Vpr Luciferase Reporter Vector (pNL4-3.Luc.R-E-) obtained from Nathaniel Landau. We are thankful to Dominic Filion for developing the algorithm for image-assisted plaque quantification. JJ is supported by the CIHR Postdoctoral Fellowship (HIV-435243-73284). We also thank Dr Annik Prat (IRCM) for the design of the summary model shown in Fig. 7. Finally, we would like to thank Mrs. Habiba Oueslati and Brigitte Mary for ther excellent editorial help and organization of the manuscript.

AUTHOR CONTRIBUTIONS

RE made all the original critical experiments revealing the role of the PCs in spike processing and the effect of their inhibitors. JJ performed all the cell assays with infectious SARS-CoV-2. DSR participated in the biochemical characterizations of TMPRSS2 processing of ACE2 and S1. UA performed all cell-to-cell fusion assays. AE made all the mutants used in the work. RMD generated the HeLa-ACE2 cells and prepared all the cells for *ex vivo* analyses. DNH performed all the immunocytochemical experiments. FD and ML performed experiments related to SARS-CoV-2 pseudovirions. AD and PSO performed all the Furin and TMPRSS2 *in vitro* kinetic cleavage analyses of peptides mimicking the S1/S2 and S2' sites. CM and KW provided the BOS-inhibitors

762 and their characterization. ED made seminal contributions to the possible role of Furin-like
763 enzymes in the processing of the spike-glycoprotein and actively contributed to the
764 conceptualization and writing of the manuscript. TNQP designed, performed, and analyzed
765 experiments related to viral entry and contributed to the writing of the manuscript. EAC (virology)
766 and NGS (biochemistry and cell biology) conceptualized the research program and provided the
767 intellectual contributions and funding for the whole project. All authors actively contributed to the
768 final version of the manuscript.

769

770 **REFERENCES**

771

772 1. Dobson AP, Carper ER. 1996. Infectious Diseases and Human Population History:
773 Throughout history the establishment of disease has been a side effect of the growth of
774 civilization. Bioscience 46:115-126.

775 2. Cui J, Li F, Shi ZL. 2019. Origin and evolution of pathogenic coronaviruses. Nat Rev
776 Microbiol 17:181-192.

777 3. Almeida JD, Tyrrell DA. 1967. The morphology of three previously uncharacterized
778 human respiratory viruses that grow in organ culture. J Gen Virol 1:175-8.

779 4. Belouzard S, Millet JK, Licitra BN, Whittaker GR. 2012. Mechanisms of coronavirus cell
780 entry mediated by the viral spike protein. Viruses 4:1011-33.

781 5. Liu PP, Blet A, Smyth D, Li H. 2020. The Science Underlying COVID-19: Implications
782 for the Cardiovascular System. Circulation 142:68-78.

783 6. Usul Afsar C. 2020. 2019-nCoV-SARS-CoV-2 (COVID-19) infection: Crucıalıty of Furın
784 and relevance wıth cancer. Med Hypotheses 140:109770.

785 7. Braun E, Sauter D. 2019. Furin-mediated protein processing in infectious diseases and
786 cancer. Clin Transl Immunology 8:e1073.

787 8. Izaguirre G. 2019. The Proteolytic Regulation of Virus Cell Entry by Furin and Other
788 Proprotein Convertases. Viruses 11.

789 9. Seidah NG, Pasquato A, Andreo U. 2021. How Do Enveloped Viruses Exploit the
790 Secretory Proprotein Convertases to Regulate Infectivity and Spread? Viruses 13:1229.

791 10. Coutard B, Valle C, de Lamballerie X, Canard B, Seidah NG, Decroly E. 2020. The spike
792 glycoprotein of the new coronavirus 2019-nCoV contains a furin-like cleavage site absent
793 in CoV of the same clade. Antiviral Res 176:104742.

11. Tang T, Bidon M, Jaimes JA, Whittaker GR, Daniel S. 2020. Coronavirus membrane fusion mechanism offers as a potential target for antiviral development. Antiviral Res doi:10.1016/j.antiviral.2020.104792:104792.

12. Hoffmann M, Kleine-Weber H, Pöhlmann S. 2020. A Multibasic Cleavage Site in the Spike Protein of SARS-CoV-2 Is Essential for Infection of Human Lung Cells. Mol Cell 78:779-784.e5.

13. Lan J, Ge J, Yu J, Shan S, Zhou H, Fan S, Zhang Q, Shi X, Wang Q, Zhang L, Wang X. 2020. Structure of the SARS-CoV-2 spike receptor-binding domain bound to the ACE2 receptor. Nature 581:215-220.

14. Lu G, Wang Q, Gao GF. 2015. Bat-to-human: spike features determining 'host jump' of coronaviruses SARS-CoV, MERS-CoV, and beyond. Trends Microbiol 23:468-78.

15. Millet JK, Whittaker GR. 2018. Physiological and molecular triggers for SARS-CoV membrane fusion and entry into host cells. Virology 517:3-8.

16. Ou X, Liu Y, Lei X, Li P, Mi D, Ren L, Guo L, Guo R, Chen T, Hu J, Xiang Z, Mu Z, Chen X, Chen J, Hu K, Jin Q, Wang J, Qian Z. 2020. Characterization of spike glycoprotein of SARS-CoV-2 on virus entry and its immune cross-reactivity with SARS-CoV. Nat Commun 11:1620.

17. Shang J, Wan Y, Luo C, Ye G, Geng Q, Auerbach A, Li F. 2020. Cell entry mechanisms of SARS-CoV-2. Proc Natl Acad Sci U S A 117:11727-11734.

18. Bestle D, Heindl MR, Limburg H, Van Lam van T, Pilgram O, Moulton H, Stein DA, Hardes K, Eickmann M, Dolnik O, Rohde C, Klenk HD, Garten W, Steinmetzer T, Böttcher-Friebertshäuser E. 2020. TMPRSS2 and furin are both essential for proteolytic activation of SARS-CoV-2 in human airway cells. Life Sci Alliance 3.

19. Mykytyn AZ, Breugem TI, Riesebosch S, Schipper D, van den Doel PB, Rottier RJ, Lamers MM, Haagmans BL. 2021. SARS-CoV-2 entry into human airway organoids is serine protease-mediated and facilitated by the multibasic cleavage site. Elife 10.

20. Seidah NG, Prat A. 2012. The biology and therapeutic targeting of the proprotein convertases. Nat Rev Drug Discov 11:367-383.

21. Van de Ven WJ, Creemers JW, Roebroek AJ. 1991. Furin: the prototype mammalian subtilisin-like proprotein-processing enzyme. Endoproteolytic cleavage at paired basic residues of proproteins of the eukaryotic secretory pathway. Enzyme 45:257-270.

22. Moulard M, Decroly E. 2000. Maturation of HIV envelope glycoprotein precursors by cellular endoproteases. Biochim Biophys Acta 1469:121-132.

23. Millet JK, Whittaker GR. 2015. Host cell proteases: Critical determinants of coronavirus tropism and pathogenesis. Virus Res 202:120-34.

24. Hoffmann M, Kleine-Weber H, Schroeder S, Kruger N, Herrler T, Erichsen S, Schiergens TS, Herrler G, Wu NH, Nitsche A, Muller MA, Drosten C, Pohlmann S. 2020. SARS-CoV-2 Cell Entry Depends on ACE2 and TMPRSS2 and Is Blocked by a Clinically Proven Protease Inhibitor. Cell 181:271-280.e8.

25. Xia S, Lan Q, Su S, Wang X, Xu W, Liu Z, Zhu Y, Wang Q, Lu L, Jiang S. 2020. The role of furin cleavage site in SARS-CoV-2 spike protein-mediated membrane fusion in the presence or absence of trypsin. Signal Transduct Target Ther 5:92.

26. Johnson BA, Xie X, Bailey AL, Kalveram B, Lokugamage KG, Muruato A, Zou J, Zhang X, Juelich T, Smith JK, Zhang L, Bopp N, Schindewolf C, Vu M, Vanderheiden A, Winkler ES, Swetnam D, Plante JA, Aguilar P, Plante KS, Popov V, Lee B, Weaver SC, Suthar MS, Routh AL, Ren P, Ku Z, An Z, Debbink K, Diamond MS, Shi PY, Freiberg AN,

840 Menachery VD. 2021. Loss of furin cleavage site attenuates SARS-CoV-2 pathogenesis.
841 Nature doi:10.1038/s41586-021-03237-4.
842 27. Peacock TP, Goldhill DH, Zhou J, Baillon L, Frise R, Swann OC, Kugathasan R, Penn R,
843 Brown JC, Sanchez-David RY, Braga L, Williamson MK, Hassard JA, Staller E, Hanley
844 B, Osborn M, Giacca M, Davidson AD, Matthews DA, Barclay WS. 2021. The furin
845 cleavage site in the SARS-CoV-2 spike protein is required for transmission in ferrets. Nat
846 Microbiol doi:10.1038/s41564-021-00908-w.
847 28. Johnson BA, Xie X, Bailey AL, Kalveram B, Lokugamage KG, Muruato A, Zou J, Zhang
848 X, Juelich T, Smith JK, Zhang L, Bopp N, Schindewolf C, Vu M, Vanderheiden A, Winkler
849 ES, Swetnam D, Plante JA, Aguilar P, Plante KS, Popov V, Lee B, Weaver SC, Suthar
850 MS, Routh AL, Ren P, Ku Z, An Z, Debbink K, Diamond MS, Shi PY, Freiberg AN,
851 Menachery VD. 2021. Loss of furin cleavage site attenuates SARS-CoV-2 pathogenesis.
852 Nature 591:293-299.
853 29. Afar DE, Vivanco I, Hubert RS, Kuo J, Chen E, Saffran DC, Raitano AB, Jakobovits A.
854 2001. Catalytic cleavage of the androgen-regulated TMPRSS2 protease results in its
855 secretion by prostate and prostate cancer epithelia. Cancer Res 61:1686-92.
856 30. Shrimp JH, Kales SC, Sanderson PE, Simeonov A, Shen M, Hall MD. 2020. An Enzymatic
857 TMPRSS2 Assay for Assessment of Clinical Candidates and Discovery of Inhibitors as
858 Potential Treatment of COVID-19. bioRxiv doi:10.1101/2020.06.23.167544.
859 31. Kawase M, Shirato K, van der Hoek L, Taguchi F, Matsuyama S. 2012. Simultaneous
860 treatment of human bronchial epithelial cells with serine and cysteine protease inhibitors
861 prevents severe acute respiratory syndrome coronavirus entry. J Virol 86:6537-45.

862 32. Nimishakavi S, Raymond WW, Gruenert DC, Caughey GH. 2015. Divergent Inhibitor
863 Susceptibility among Airway Lumen-Accessible Tryptic Proteases. PLoS One
864 10:e0141169.
865 33. Hörnich BF, Großkopf AK, Schlagowski S, Tenbusch M, Kleine-Weber H, Neipel F,
866 Stahl-Hennig C, Hahn AS. 2021. SARS-CoV-2 and SARS-CoV spike-mediated cell-cell
867 fusion differ in the requirements for receptor expression and proteolytic activation. J Virol
868 doi:10.1128/jvi.00002-21.
869 34. Cyranoski D. 2020. Profile of a killer: the complex biology powering the coronavirus
870 pandemic. Nature 581:22-26.
871 35. Matoba Y, Aoki Y, Tanaka S, Yahagi K, Katsushima Y, Katsushima F, Sugawara K,
872 Matsuzaki Y, Mizuta K. 2016. HeLa-ACE2-TMPRSS2 Cells Are Useful for the Isolation
873 of Human Coronavirus 229E. Jpn J Infect Dis 69:452-4.
874 36. Thomas G. 2002. Furin at the cutting edge: from protein traffic to embryogenesis and
875 disease. Nature Reviews Molecular Cell Biology 3:753-766.
876 37. Örd M, Faustova I, Loog M. 2020. Biochemical evidence of furin specificity and potential
877 for phospho-regulation at Spike protein S1/S2 cleavage site in SARS-CoV2 but not in
878 SARS-CoV1 or MERS-CoV. bioRxiv
879 doi:10.1101/2020.06.23.166900:2020.06.23.166900.
880 38. Andersen KG, Rambaut A, Lipkin WI, Holmes EC, Garry RF. 2020. The proximal origin
881 of SARS-CoV-2. Nat Med 26:450-452.
882 39. Schjoldager KT, Clausen H. 2012. Site-specific protein O-glycosylation modulates
883 proprotein processing - deciphering specific functions of the large polypeptide GalNAc-
884 transferase gene family. Biochim Biophys Acta 1820:2079-2094.

40. Benton DJ, Wrobel AG, Xu P, Roustan C, Martin SR, Rosenthal PB, Skehel JJ, Gamblin SJ. 2020. Receptor binding and priming of the spike protein of SARS-CoV-2 for membrane fusion. Nature 588:327-330.

41. Belouzard S, Chu VC, Whittaker GR. 2009. Activation of the SARS coronavirus spike protein via sequential proteolytic cleavage at two distinct sites. Proc Natl Acad Sci U S A 106:5871-6.

42. Hallenberger S, Bosch V, Angliker H, Shaw E, Klenk HD, Garten W. 1992. Inhibition of furin-mediated cleavage activation of HIV-1 glycoprotein gp160. Nature 360:358-361.

43. Susan-Resiga D, Essalmani R, Hamelin J, Asselin MC, Benjannet S, Chamberland A, Day R, Szumska D, Constam D, Bhattacharya S, Prat A, Seidah NG. 2011. Furin Is the Major Processing Enzyme of the Cardiac-specific Growth Factor Bone Morphogenetic Protein 10. J Biol Chem 286:22785-22794.

44. Cheng YW, Chao TL, Li CL, Chiu MF, Kao HC, Wang SH, Pang YH, Lin CH, Tsai YM, Lee WH, Tao MH, Ho TC, Wu PY, Jang LT, Chen PJ, Chang SY, Yeh SH. 2020. Furin Inhibitors Block SARS-CoV-2 Spike Protein Cleavage to Suppress Virus Production and Cytopathic Effects. Cell Rep 33:108254.

45. Walls AC, Park YJ, Tortorici MA, Wall A, McGuire AT, Veesler D. 2020. Structure, Function, and Antigenicity of the SARS-CoV-2 Spike Glycoprotein. Cell 181:281-292.e6.

46. Hoffmann M, Mösbauer K, Hofmann-Winkler H, Kaul A, Kleine-Weber H, Krüger N, Gassen NC, Müller MA, Drosten C, Pöhlmann S. 2020. Chloroquine does not inhibit infection of human lung cells with SARS-CoV-2. Nature 585:588-590.

47. Vincent MJ, Bergeron E, Benjannet S, Erickson BR, Rollin PE, Ksiazek TG, Seidah NG, Nichol ST. 2005. Chloroquine is a potent inhibitor of SARS coronavirus infection and spread. Virol J 2:69.

909 48. Bayati A, Kumar R, Francis V, McPherson PS. 2021. SARS-CoV-2 infects cells following
910 viral entry via clathrin-mediated endocytosis. J Biol Chem 296:100306.
911 49. Platt EJ, Wehrly K, Kuhmann SE, Chesebro B, Kabat D. 1998. Effects of CCR5 and CD4
912 cell surface concentrations on infections by macrophagetropic isolates of human
913 immunodeficiency virus type 1. J Virol 72:2855-64.
914 50. Plante JA, Mitchell BM, Plante KS, Debbink K, Weaver SC, Menachery VD. 2021. The
915 variant gambit: COVID-19's next move. Cell Host Microbe 29:508-515.
916 51. Peacock TP, Penrice-Randal R, Hiscox JA, Barclay WS. 2021. SARS-CoV-2 one year on:
917 evidence for ongoing viral adaptation. J Gen Virol 102.
918 52. Rajah MM, Hubert M, Bishop E, Saunders N, Robinot R, Grzelak L, Planas D, Dufloo J,
919 Gellenoncourt S, Bongers A, Zivaljic M, Planchais C, Guivel-Benhassine F, Porrot F,
920 Mouquet H, Chakrabarti LA, Buchrieser J, Schwartz O. 2021. SARS-CoV-2 Alpha, Beta,
921 and Delta variants display enhanced Spike-mediated syncytia formation. EMBO J
922 doi:10.15252/embj.2021108944:e108944.
923 53. Matsuyama S, Nagata N, Shirato K, Kawase M, Takeda M, Taguchi F. 2010. Efficient
924 activation of the severe acute respiratory syndrome coronavirus spike protein by the
925 transmembrane protease TMPRSS2. J Virol 84:12658-64.
926 54. Heurich A, Hofmann-Winkler H, Gierer S, Liepold T, Jahn O, Pöhlmann S. 2014.
927 TMPRSS2 and ADAM17 cleave ACE2 differentially and only proteolysis by TMPRSS2
928 augments entry driven by the severe acute respiratory syndrome coronavirus spike protein.
929 J Virol 88:1293-307.
930 55. Monteil V, Kwon H, Prado P, Hagelkrüys A, Wimmer RA, Stahl M, Leopoldi A, Garreta
931 E, Hurtado Del Pozo C, Prosper F, Romero JP, Wirnsberger G, Zhang H, Slutsky AS,
932 Conder R, Montserrat N, Mirazimi A, Penninger JM. 2020. Inhibition of SARS-CoV-2

933 Infections in Engineered Human Tissues Using Clinical-Grade Soluble Human ACE2. Cell
934 181:905-913.e7.
935 56. Hoffmann M, Mösbauer K, Hofmann-Winkler H, Kaul A, Kleine-Weber H, Krüger N,
936 Gassen NC, Müller MA, Drosten C, Pöhlmann S. 2020. Chloroquine does not inhibit
937 infection of human lung cells with SARS-CoV-2. Nature doi:10.1038/s41586-020-2575-3.
938 57. Bellamine A, Pham TNQ, Jain J, Wilson J, Sahin K, Dallaire F, Seidah NG, Durkee S,
939 Radošević K, Cohen É A. 2021. L-Carnitine Tartrate Downregulates the ACE2 Receptor
940 and Limits SARS-CoV-2 Infection. Nutrients 13.
941 58. Padmanabhan P, Desikan R, Dixit NM. 2020. Targeting TMPRSS2 and Cathepsin B/L
942 together may be synergistic against SARS-CoV-2 infection. PLoS Comput Biol
943 16:e1008461.
944 59. Papa G, Mallery DL, Albecka A, Welch LG, Cattin-Ortolá J, Luptak J, Paul D, McMahon
945 HT, Goodfellow IG, Carter A, Munro S, James LC. 2021. Furin cleavage of SARS-CoV-
946 2 Spike promotes but is not essential for infection and cell-cell fusion. PLoS Pathog
947 17:e1009246.
948 60. Altulea D, Maassen S, Baranov MV, van den Bogaart G. 2021. What makes
949 (hydroxy)chloroquine ineffective against COVID-19: insights from cell biology. J Mol
950 Cell Biol doi:10.1093/jmcb/mjab016.
951 61. Self WH, Semler MW, Leither LM, Casey JD, Angus DC, Brower RG, Chang SY, Collins
952 SP, Eppensteiner JC, Filbin MR, Files DC, Gibbs KW, Ginde AA, Gong MN, Harrell FE,
953 Jr, Hayden DL, Hough CL, Johnson NJ, Khan A, Lindsell CJ, Matthay MA, Moss M, Park
954 PK, Rice TW, Robinson BRH, Schoenfeld DA, Shapiro NI, Steingrub JS, Ulysse CA,
955 Weissman A, Yealy DM, Thompson BT, Brown SM, National Heart L, Network BIPCT.

2020. Effect of Hydroxychloroquine on Clinical Status at 14 Days in Hospitalized Patients With COVID-19: A Randomized Clinical Trial. JAMA 324:2165-2176.

62. Rosenke K, Jarvis MA, Feldmann F, Schwarz B, Okumura A, Lovaglio J, Saturday G, Hanley PW, Meade-White K, Williamson BN, Hansen F, Perez-Perez L, Leventhal S, Tang-Huau TL, Callison J, Haddock E, Stromberg KA, Scott D, Sewell G, Bosio CM, Hawman D, de Wit E, Feldmann H. 2020. Hydroxychloroquine prophylaxis and treatment is ineffective in macaque and hamster SARS-CoV-2 disease models. JCI Insight 5.

63. Glowacka I, Bertram S, Müller MA, Allen P, Soilleux E, Pfefferle S, Steffen I, Tsegaye TS, He Y, Gnirss K, Niemeyer D, Schneider H, Drosten C, Pöhlmann S. 2011. Evidence that TMPRSS2 activates the severe acute respiratory syndrome coronavirus spike protein for membrane fusion and reduces viral control by the humoral immune response. J Virol 85:4122-34.

64. Raghuvamsi PV, Tulsian NK, Samsudin F, Qian X, Purushotorman K, Yue G, Kozma MM, Hwa WY, Lescar J, Bond PJ, MacAry PA, Anand GS. 2021. SARS-CoV-2 S protein:ACE2 interaction reveals novel allosteric targets. Elife 10.

65. Zhang H, Wada J, Hida K, Tsuchiyama Y, Hiragushi K, Shikata K, Wang H, Lin S, Kanwar YS, Makino H. 2001. Collectrin, a collecting duct-specific transmembrane glycoprotein, is a novel homolog of ACE2 and is developmentally regulated in embryonic kidneys. J Biol Chem 276:17132-9.

66. Yan R, Zhang Y, Li Y, Xia L, Guo Y, Zhou Q. 2020. Structural basis for the recognition of SARS-CoV-2 by full-length human ACE2. Science 367:1444-1448.

67. Yamamoto M, Kiso M, Sakai-Tagawa Y, Iwatsuki-Horimoto K, Imai M, Takeda M, Kinoshita N, Ohmagari N, Gohda J, Semba K, Matsuda Z, Kawaguchi Y, Kawaoka Y, Inoue JI. 2020. The Anticoagulant Nafamostat Potently Inhibits SARS-CoV-2 S Protein-

Mediated Fusion in a Cell Fusion Assay System and Viral Infection In Vitro in a Cell-Type-Dependent Manner. Viruses 12.

68. Koch J, Uckeley ZM, Doldan P, Stanifer M, Boulant S, Lozach PY. 2021. TMPRSS2 expression dictates the entry route used by SARS-CoV-2 to infect host cells. EMBO J 40:e107821.

69. Wölfel R, Corman VM, Guggemos W, Seilmaier M, Zange S, Müller MA, Niemeyer D, Jones TC, Vollmar P, Rothe C, Hoelscher M, Bleicker T, Brünink S, Schneider J, Ehmann R, Zwirglmaier K, Drosten C, Wendtner C. 2020. Virological assessment of hospitalized patients with COVID-2019. Nature 581:465-469.

70. Zhou L, Niu Z, Jiang X, Zhang Z, Zheng Y, Wang Z, Zhu Y, Gao L, Huang H, Wang X, Sun Q. 2020. The SARS-CoV-2 targets by the pscRNA profiling of ACE2, TMPRSS2 and Furin proteases. iScience doi:10.1016/j.isci.2020.101744:101744.

71. Mayer G, Boileau G, Bendayan M. 2004. Sorting of furin in polarized epithelial and endothelial cells: expression beyond the Golgi apparatus. J Histochem Cytochem 52:567-580.

72. Antalis TM, Bugge TH, Wu Q. 2011. Membrane-anchored serine proteases in health and disease. Prog Mol Biol Transl Sci 99:1-50.

73. Chu H, Chan JF, Yuen TT, Shuai H, Yuan S, Wang Y, Hu B, Yip CC, Tsang JO, Huang X, Chai Y, Yang D, Hou Y, Chik KK, Zhang X, Fung AY, Tsoi HW, Cai JP, Chan WM, Ip JD, Chu AW, Zhou J, Lung DC, Kok KH, To KK, Tsang OT, Chan KH, Yuen KY. 2020. Comparative tropism, replication kinetics, and cell damage profiling of SARS-CoV-2 and SARS-CoV with implications for clinical manifestations, transmissibility, and laboratory studies of COVID-19: an observational study. Lancet Microbe 1:e14-e23.

1003 74. Gunst JD, Staerke NB, Pahus MH, Kristensen LH, Bodilsen J, Lohse N, Dalgaard LS,
1004 Brønnum D, Fröbert O, Hønge B, Johansen IS, Monrad I, Erikstrup C, Rosendal R, Vilstrup
1005 E, Mariager T, Bove DG, Offersen R, Shakar S, Cajander S, Jørgensen NP, Sritharan SS,
1006 Breining P, Jespersen S, Mortensen KL, Jensen ML, Kolte L, Frattari GS, Larsen CS,
1007 Storgaard M, Nielsen LP, Tolstrup M, Sædder EA, Østergaard LJ, Ngo HTT, Jensen MH,
1008 Højen JF, Kjolby M, Søgaard OS. 2021. Efficacy of the TMPRSS2 inhibitor camostat
1009 mesilate in patients hospitalized with Covid-19-a double-blind randomized controlled trial.
1010 EClinicalMedicine 35:100849.
1011 75. Shapira T, Monreal IA, Dion SP, Jager M, Désilets A, Olmstead AD, Vandal T, Buchholz
1012 DW, Imbiakha B, Gao G, Chin A, Rees WD, Steiner T, Nabi IR, Marsault E, Sahler J,
1013 August A, Van de Walle G, Whittaker GR, Boudreault PL, Aguilar HC, Leduc R, Jean F.
1014 2021. A novel highly potent inhibitor of TMPRSS2-like proteases blocks SARS-CoV-2
1015 variants of concern and is broadly protective against infection and mortality in mice.
1016 bioRxiv doi:10.1101/2021.05.03.442520.
1017 76. Ou T, Mou H, Zhang L, Ojha A, Choe H, Farzan M. 2021. Hydroxychloroquine-mediated
1018 inhibition of SARS-CoV-2 entry is attenuated by TMPRSS2. PLoS Pathog 17:e1009212.
1019 77. Morens DM, Fauci AS. 2020. Emerging Pandemic Diseases: How We Got to COVID-19.
1020 Cell 183:837.
1021 78. Lodge R, Lalonde JP, Lemay G, Cohen EA. 1997. The membrane-proximal
1022 intracytoplasmic tyrosine residue of HIV-1 envelope glycoprotein is critical for basolateral
1023 targeting of viral budding in MDCK cells. EMBO J 16:695-705.
1024 79. Forget J, Yao XJ, Mercier J, Cohen EA. 1998. Human immunodeficiency virus type 1 vpr
1025 protein transactivation function: mechanism and identification of domains involved. J Mol
1026 Biol 284:915-23.

80. Schmidt F, Weisblum Y, Muecksch F, Hoffmann HH, Michailidis E, Lorenzi JCC, Mendoza P, Rutkowska M, Bednarski E, Gaebler C, Agudelo M, Cho A, Wang Z, Gazumyan A, Cipolla M, Caskey M, Robbiani DF, Nussenzweig MC, Rice CM, Hatziioannou T, Bieniasz PD. 2020. Measuring SARS-CoV-2 neutralizing antibody activity using pseudotyped and chimeric viruses. J Exp Med 217.

FIGURE LEGENDS

Figure 1: **Processing of S-peptides by Furin and TMPRSS2. (A)** Schematic representation of the primary structure of preproS and its domains and the predicted Furin-like S1/S2 site generating the S1- and S2-subunits, as well as the S2' site preceding the fusion peptide (FP). The signal peptide (SP), N-terminal domain (NTD), receptor binding domain (RBD) to ACE2, the two heptad repeats HR1 and HR2, the transmembrane domain (TM), the cytosolic tail (CT) and the C-terminal V5-tag are indicated. **(B)** *In vitro* Furin activity against peptides mimicking the S1/S2 (and its mutants) and S2' cleavage site sequence of the spike protein from SARS-CoV-2 and SARS-CoV-1, as described in SI-Table 1. Each substrate was tested at a final protease concentration of 2 and 100 nM. **(C)** *In vitro* TMPRSS2 activity (at 50 nM) against peptides mimicking the S1/S2 and S2' cleavage site sequence of the spike protein from SARS-CoV-2 (and its mutants) described in SI-Table 1.

Figure 2: **Processing of spike-glycoprotein in HeLa cells.** (**A**) Western blot analyses of the processing of WT proS into V5-tagged S2 and S2' by the proprotein convertases Furin, PC5A, PACE4 and PC7 following co-transfection of their cDNAs in HeLa cells. The migration positions of immature $proS_{im}$, S2 and S2' as well as the actin loading control are emphasized. V = empty pIRES-EGFP-V5 vector. (**B**) Western blot analyses of HeLa cells following co-transfection with cDNAs coding for either WT-S-protein or its double Ala-mutant [R685A + R682A] (μS1/S2) in the absence or presence of Furin cDNA at a ratio S:protease = 1:2. *Inconsistently observed oligomeric forms of proS. (**C**) Identification of S2' cleavage site by MS/MS. WT-spike-glycoprotein was immunoprecipitated from HeLa cells using V5 agarose beads then resolved by SDS electrophoresis SDS/PAGE and subjected to silver staining (left panel); the positions of the slices are indicated (1 to 10). The MS/MS analysis of peptides generated by a Lys-specific protease

(K$_{814}$↓) are indicated; the data represent the ratio of SFIEDLLFNK825 to R$_{815}$SFIEDLLFNK$_{825}$ (right panel). (**D**) Western blot analyses of HeLa cells co-transfected with V5-tagged spike protein, WT (S) or its Furin-optimized S2' (KRRKR$_{815}$↓SF) mutant (μS2'), and empty vector (V) or Furin. (**A, B**) The estimated % cleavages into S1/S2 and S2' are shown and were calculated as the ratio of the V5-immunoreactivity of the cleaved form to the sum of all forms. The data are representative of at least three independent experiments.

Figure 3: **Processing of spike-glycoprotein at S2' is enhanced in presence of ACE2.** Western blot showing the impact of ACE2 on the processing of WT and μS1/S2 spike-glycoproteins by Furin. HeLa cells expressing empty vector (V), WT proS (**A**) or its μS1/S2 mutant (**B**) without or with Furin, ACE2 or both were analysed by Western blotting using anti-V5 antibody. The ratio of cDNAs used was S:ACE2:Furin = 1:1:1. The data are representative of at least three independent experiments.

Figure 4: **Inhibition of PCs by BOS compounds.** (**A**) Chemical motif of BOS-inhibitors and representative structure of BOS-318. (**B**) *In vitro* BOS-inhibition of the cleavage of the fluorogenic dibasic substrate FAM-QRVRRAVGIDK-TAMRA by each of the proprotein convertases Furin, PC5 (PCSK5), PACE4 (PCSK6) and PC7 (PCSK7). All experiments were performed in 10 different wells and the average pIC$_{50}$ (in nM) was calculated. Shown for comparison is the inhibitory pIC$_{50}$ of the Furin-like inhibitor RVKR-cmk performed >100 times. (**C**) *In vitro* inhibition of Furin by the BOS compounds. Furin (2 nM) was incubated with increasing concentration of BOS-inhibitors, and its enzymatic activity against the synthetic peptides DABSYL/Glu-TNSP**RR**A**R**↓SVAS-EDANS (5 μM) was measured at pH 7.5 (n=3). (**D**) Golgi assay: table representing the effects of BOS-inhibitors on U2OS cells expressing each of Furin, PC5A, PACE4 and PC7 simultaneously transduced with a BacMam-delivered construct

containing a Golgi-targeting sequence followed by a 12-amino acid Furin/PCSK cleavage site from Bone Morphogenic Protein 10 (BMP10) and GFP at the C terminus (GalNAc-T2-GGGGS-DSTARIRR↓NAKG-GGGGS-GFP). Dibasic cleavage releases NAKG-GGGGS-GFP thereby reducing the Golgi-associated fluorescence estimated by imaging. (**E**) Furin-inhibitors (BOS) abrogate endogenous processing of the spike-glycoprotein. Hela cells were transiently transfected with a cDNA encoding an empty vector (V) or with one expressing the V5-tagged spike (S) glycoprotein (spike-V5). At 5h pre-transfection, cells were treated with vehicle DMSO (NT, duplicate) or with the Furin-inhibitors at indicated concentrations, or RVKR-cmk at 50 μM. At 24h post-transfection media were replaced with fresh ones lacking (NT) or containing the inhibitors for an additional 24h. Cell extracts were analyzed by Western blotting using a mAb-V5. All data are representative of at least three independent experiments.

Figure 5: **Furin-like inhibitors and Camostat treatment decrease SARS-CoV-2 infection in Calu-3 Cells.** (**A**) Replication kinetics was studied at 12, 24 and 48h post-infection by plaque assay to determine PFUs of SARS-CoV-2 virus in the supernatant of infected Calu-3 cells treated or not with 1μM BOS-318, BOS-857 and BOS-981. A line graph represents results of the triplicate plaque assay results (mean ± SD). (**B**) The virus titers (PFU per milliliter) released in the supernatant (24h post-infection) of infected Calu-3 cells treated with indicated concentrations of BOS-318 were determined by plaque assay (mean ± SD of triplicates, *$p < 0.05$; **$p < 0.01$; ***$p < 0.001$) (left panel). The selectivity index (SI) of BOS-318 in Calu-3 cells as shown in top right panel was determined by CC_{50}/IC_{50}. The left y axis indicates the inhibition of virus titer (percent) relative to that of the untreated control group (red). The right y axis indicates the cell viability (percent) relative to that of the untreated control group (green). The CC_{50} (50% cytotoxic concentration), IC_{50} (half maximal inhibitory concentration), and SI (selectivity index) values for

each inhibitor are as shown. Representative plaque images of infected Calu-3 cells treated with indicated doses of BOS-inhibitors are shown in the bottom right panel. (**C**) Immunoblots for the infected Calu-3 cells (right panel) and viral particles secreted in the supernatant (left panel) with and without treatment with BOS-inhibitors indicate reduced viral protein levels. Immunoblots were probed for the full-length (proSm) and cleaved (S2) fragments of viral S protein and nucleocapsid (N) protein as indicated; β-Actin was included as the loading control for the cells. (**D**) The virus titers (PFU per milliliter) released in the supernatant (24h post-infection) of infected Calu-3 cells treated with BOS-318 and/or Camostat (Camo) were determined by plaque assay (mean ± SD of duplicates, *, $p < 0.05$; **, $p < 0.01$; ***, $p < 0.001$) (top panel). Representative plaque images of infected Calu-3 cells are shown in the bottom panel. Color plaques differentiate the lawn (one color gray per well) from individual plaques (independent colors).

Figure 6: **Processing of SARS-CoV-2 S by Furin-like convertases and TMPRSS2 is critical for viral entry in human lung epithelial cells but not in model HEK293 cells stably expressing ACE2**. (**A**) Furin cleavage of proS at the S1/S2 site is required for SARS-CoV-2 pseudoviral entry in Calu-3 cells but not HEK293T-ACE2 cells. Cells were inoculated with nanoluciferase-expressing HIV particles pseudotyped with SARS-CoV-2: wild-type spike (WT), double Ala-mutant spike (μS1/S2) or Furin-optimized spike (μS2'). Inhibition of proS processing at S1/S2 by a novel Furin-like inhibitor (BOS-318) during pseudovirion packaging prevents viral entry in Calu-3 cells but not in HEK293T-ACE2 cells. (**B**) Western blot analyses show inhibition by BOS-318 of proS processing at S1/S2 site. Purified pseudovirions and cellular extracts of producing HEK293-T17 cells treated or not with BOS-318 inhibitor were separated on SDS-PAGE gel and analyzed for HIV-1 p24 and V5-tagged S-protein (proSm or cleaved, S2) as indicated. (**C**) Pre-treatment of Calu-3 cells with (B) 1 μM BOS-318, (C) 100 μM Camostat or both (B+C) markedly

reduces viral entry. In Panels A and C, Calu-3 cells were transduced with nanoluciferase-expressing HIV particles pseudotyped with SARS-CoV-2 S WT, μS1/S2 or μS2' for 72h and analyzed for nano-luciferase expression. Viral entry was expressed as fold increase over that given by bald particles (pseudovirions made in the absence of S). In panels **A** and **C** each dot represents a different experiment with median luciferase activity calculated from three biological replicates. Two to four experiments were performed for each cell type. Error bars indicate standard deviation (SD) from the mean.

Figure 7: **Spike-induced cell-to-cell fusion relies on Furin cleavage at S1/S2.** (**A**) Cell-to-cell fusion between donor cells (HeLa) expressing the fusogenic SARS-CoV-2 spike protein along with the HIV trans-activator Tat, and acceptor cells (TZM-bl) that express ACE2. Upon fusion, Tat is transferred from donor to acceptor cells, thereby inducing luciferase expression. (**B**) Cell-to-cell fusion was evaluated using confocal microscopy. A representative immunocytochemistry of Hela cells transfected with a vector expressing SARS-CoV-2 spike co-cultured with TZM-bl cells for 18h. The number of syncytia (multiple nuclei) was examined using CellMask™ to probe for the plasma membrane and Dapi to stain the nuclei. (**C**) Donor cells were transfected with vectors expressing either no protein (empty vector, V), μS1/S2, or WT-spike (S) in the absence (NT) or presence of vehicle (DMSO) or with the Furin-inhibitors BOS-318, BOS-981, BOS-857 (300 nM) or RVKR (10 μM). Acceptor cells were transfected with a vector expressing ACE2. After 48h, donor and acceptor cells were co-cultured for 18h. Relative luminescence units (RLU) were normalized to the V value arbitrarily set to 1. Data are presented as mean values ± SD (n=3), One-Way ANOVA, Dunn-Sidàk multiple comparison test. (**D**) Donor HeLa cells expressing WT-S or its indicated mutants and variants were co-cultured with acceptor TZM-bl cells expressing ACE2. The extent of fusion is represented as a ratio between the RLU measured for each condition

and that of donor cells expressing empty vector. The bar graph represents the average of 3 experiments performed in triplicates. Data are presented as mean values ± SEM (n=3), One-way Anova Bonferroni multiple comparison test. Two-Way ANOVA, Dunn-Sidàk multiple comparison test.

Figure 8: **Spike-glycoprotein processing by Furin and TMPRSS2 in a co-culture system and their role in cell-to-cell fusion.** Donor HeLa cells expressing empty vector (V), WT-S-HA or μS1/S2-HA were co-cultured with acceptor TZM-bl cells expressing V, ACE2, or ACE2 + TMPRSS2 (TMP). From the same experiment, cell-to-cell fusion (**A**) was assessed in parallel by Western blotting of spike-glycoproteins in cells and media using an anti-V5 mAb (**B**). Secreted forms of spike protein (S1) in the media were detected with anti HA-HRP upon immunoprecipitation with anti-HA agarose. The bar graph shows one representative fusion assay done un duplicate. The corresponding Western-blot is representative of three independent experiments. Values of S2 and S2' relative to β-actin are shown (nd = too low or not detected).

Figure 9: **Exogenous TMPRSS2-generated shedding of ACE2 differentially regulates S-induced fusion at the plasma membrane of WT-S *versus* μAS1/S2.** Donor HeLa cells expressing double tagged (N-terminal HA-tag; C-terminal V5-tag) spike-glycoprotein WT (S) or its S1/S2 mutant (μAS1/S2) were co-cultured with acceptor TZM-bl cells expressing (empty vector, V), ACE2, or ACE2 + TMPRSS2 (TMP) and treated with DMSO (vehicle control) or Camostat (120 μM). Within the same experiment, cell-to-cell fusion (**A**) was assessed in parallel with spike processing in cells and media by Western-blot (**B, C**). (**A**) The extent of fusion is represented as a ratio between the RLU measured for each condition and that of donor cells expressing V. The bar graph represents the average of 2 experiments performed in triplicates. (**B, C**). Western blot analyses of media and cell extracts of the co-cultured cells with donor cells overexpressing double tagged (N-

terminal HA-tag; C-terminal V5-tag) spike-glycoprotein, WT (S) (**B**) or μAS1/S2 (**C**). The arrow points to a putative degradation product of S2', that is absent in presence of Camostat. Media were subjected to immunoprecipitation with anti-HA agarose for the secreted forms of spike protein (S1, $S1_L$) followed by Western blotting with anti HA-HRP. In the cell extracts Spike-glycoproteins and ACE2 were immunoblotted with anti-V5 mAb and a polyclonal ACE2 antibody, respectively. The data are representative of three independent experiments.

Figure 10: **The C-terminal collectrin-like domain of ACE2 may be critical for the regulation of cell-to-cell fusion of spike-glycoprotein when exogenous TMPRSS2 is present.** (**A**) Schematic representation of the primary structure of human ACE2 with emphasis on the C-terminal collectrin-like domain (aa 616-768, light gray), TMPRSS2 cleavage region (aa 697-716, black) and the polybasic amino-acid segments in which K/R were mutated to A (C0 and C4) (amino acids underlined and in bold). Also shown are the peptidase domain (aa 19-615, white) containing the regions involved in the interaction with the spike SARS-CoV protein (hatched) and transmembrane domain (TM). (**B**) HeLa cells were co-transfected with ACE2, WT (ACE2) or its mutant ACE2 (C0+C4), and TMPRSS2, WT (TMPRSS2) or its S441A active-site mutant (μTMPRSS2), or empty vector (V). Media and cell extracts were analyzed by western blotting for shed ACE2 (sACE2) and ACE2, respectively. The migration positions of the ~95 kDa and ~80 kDa sACE2 are emphasized. (**C**) Donor HeLa cells expressing WT-S-HA or μAS1/S2-HA were co-cultured with acceptor TZM-bl cells expressing ACE2, WT (ACE2) or its mutant ACE2 (C0+C4) in presence or absence of TMPRSS2. From the same experiment, cell-to-cell fusion was assessed (**C**), in parallel with WB analyses of cells and media (**D**). The extent of fusion is represented as a ratio between the RLU measured for each condition and that of donor cells expressing an empty vector. The bar graph represents the average of 3 experiments performed in triplicates. Data are presented as mean values ± SD (n=3), One-way Anova Turkey's multiple

comparison test. (**D**) Co-culture media were subjected to immunoprecipitation with anti-HA agarose for the secreted forms of spike protein (S1) followed by western blot with anti HA-HRP. Spike-glycoproteins in the cell extracts were immunoblotted with anti-V5 mAb. The Western blot data are representative of three independent experiments.

Figure 11: **Proposed model for the processing of S-protein and its blockade by Furin and TMPRSS2 inhibitors.** Boxed left panel: schematic representation of the S-glycoprotein domains of SARS-CoV-2, including the N-terminal (NTD) and C-terminal (CTD) domains of S1, the Furin-S1/S2 and the Furin/TMPRSS2-S2' processing sites as well as the fusogenic α-helix that follows S2'. Binding of the RBD domain of S1 to the membrane associated ACE2 in target cells, and the cell surface expression of TMPRSS2 and Furin are also schematized. Right panels: (**1**) BOS-inhibitors (or μS1/S2 mutant) completely prevent cell-to-cell fusion of donor Hela cells expressing S-glycoprotein with acceptor HeLa-ACE2 cells, which lack endogenous TMPRSS2. In this context, this reveals that Furin is a major processing enzyme cleaving at S1/S2 and generating S2'. (**2**) In acceptor HeLa cells expressing TMPRSS2 (+), maximal prevention of cell-to-cell fusion can be achieved by a combination of Furin (BOS, phenocopying the μS1/S2 or μAS1/S2 mutants) and TMPRSS2 (Camostat) inhibitors blocks S2' production, ACE2-shedding (sACE2) and the separation of sACE2-$S1_L$ complex from S2. (**3**) Optimal blockade of SARS-CoV-2 infection of Calu-3 cells, which express endogenously both Furin and TMPRSS2, is also achieved by a combination of Furin (BOS) and TMPRSS2 (Camostat) inhibitors.

SUPPORTING INFORMATION (SI): TABLE 1; FIGURES 1-7

Table 1: **Sequences of the different peptides mimicking the Cov spike cleavage sites that have been tested in the enzymatic assay.** The arrow indicates the expected cleavage site.

SI-Figure 1: **Importance of Furin in the processing of the Spike-glycoprotein.** (**A**) HeLa cells were first transfected with control non-targeting siRNA (siCTL) or siRNA Furin (siFur) at final concentrations of 20 nM, or mock transfected (N) and 24h later, transfected with empty vector (V) or with that coding for a V5-tagged spike-glycoprotein for an additional 48h. Following lysis, proteins were resolved on SDS-PAGE followed by WB with anti-V5 or anti-Furin antibodies. (**B**) HeLa cells transfected with empty vector (V), V5-tagged wild type spike-protein (WT) or its S1/S2 site mutant (μS1/S2) were treated with Endo-F and Endo-H or mock treated (NT) and analyzed as described in panel A. (**C, D**) HeLa cells transfected with V5-tagged wild type spike-protein (WT) or S1/S2 single mutants (**C**) or S2' single or double mutants (**D**) in the absence (V) or presence of overexpressed Furin were lysed and analyzed by WB.

SI-Figure 2: **Immunocytochemistry of the co-localization of ACE2 and S-protein or μS1/S2-S in HeLa cells.** Immunofluorescence of S-protein (green), WT (S) or μS1/S2, and ACE2 (red) were revealed using the spike S2-antibody GTX632604 in non-permeabilized (NP) conditions or anti-V5 in permeabilized (P) conditions, and ACE2 antibody AF933. The confocal co-localizations are shown in the merged Figures. Scale bar = 10 μm.

SI-Figure 3: **Furin-like inhibitors strongly reduce SARS-CoV-2 infection in Calu-3 cells.** Calu-3 cells were treated with indicated concentrations of (**A**) BOS-857 and (**B**) BOS-981 and infected with SARS-CoV-2 for 24h. Virus titers in the supernatant were determined by plaque assay on VeroE6 cells (mean plaque forming units [PFU] per ml) ± SD of triplicates, $^{*}p < 0.05$; $^{**}p < 0.01$; $^{***}p < 0.001$). The selectivity index (SI) of (**A**) BOS-857, and (**B**) BOS-981 in

Calu-3 cells as shown in top right panel was determined by CC_{50}/IC_{50}. The left y axis indicates the inhibition of virus titer (percent) relative to that of the untreated control group (red). The right y axis indicates the cell viability (percent) relative to that of the untreated control group (green). Representative plaque images of infected Calu-3 cells treated with indicated doses of BOS-inhibitors are shown in the bottom right panel. Color plaques differentiate the lawn (one color gray per well) from individual plaques (independent colors).

SI-Figure 4: **Furin-like inhibitors modestly reduce virus production in SARS-CoV-2-infected Vero E6 cells in a concentration-dependent manner. (A)** Vero E6 cells treated or not with 1µM BOS-318, BOS-857 or BOS-981 were infected with SARS-CoV-2 for up to 45h. Virus titers in the supernatant obtained at 12, 24 and 48 h post infection were determined by plaque assay on Vero E6. A line graph represents results of the triplicate plaque assay (mean PFU/ml ± SD). **(B, C, and D)** Virus released in the supernatant (48 hr post infection) of infected Vero E6 cells treated with indicated concentrations of (B) BOS-318, (C) BOS-857, or (D) BOS-981 were determined by plaque assay (mean ± SD of triplicates, $*p < 0.05$; $**p < 0.01$; $***p < 0.001$).

SI-Figure 5: **Combination of BOS-981 and Camostat reduces SARS-CoV-2 replication.** Calu-3 cells were treated with BOS-981 and/or Camostat (Camo) and infected with SARS-CoV-2 for 24h. Virus titers in the supernatant were determined by plaque assay on VeroE6 (mean PFU/ml ± SD of duplicates, $*p< 0.05$. Representative plaque images of infected Calu-3 cells are shown in the bottom panel. Color plaques differentiate the lawn (one color gray per well) from individual plaques (independent colors).

SI-Figure 6: **Cell-to-cell fusion assay: correlation between syncytia formation and luciferase activity.** (**A**) Cell-to-cell fusion between donor cells (HeLa) and acceptor cells (TZM-bl) was evaluated using confocal microscopy. Hela cells transfected with: (**a**) an empty vector (V), or

expressing (**b**) HIV-gp160 and Tat, (**c**) SARS-CoV-2 spike, or (**d**) µS1/S2 were co-cultured with TZM-bl cells for 18h and the number of syncytia was examined using CellMask™ to probe for the plasma membrane and Dapi to stain the nuclei. (**B)** Donor cells were transfected with vectors expressing either no protein (V), Tat, WT-spike (S), Tat and WT-spike (Tat + S) or Tat and HIV-gp160 (Tat + gp160). Acceptor cells were transfected with a vector expressing no protein (V), with ACE2 or directly with Tat as a positive control (hatched bar). After 48h, cells were co-cultured for 18h. Luminescence was normalized to the V value arbitrarily set to 1. Data are presented as mean values ± SD (n=3) and a representative experiment is shown. (**C)** Donor cells were transfected with increasing amount of plasmid expressing WT-spike and acceptor cells were transfected with a vector expressing ACE2. After 48h, cells were co-cultured for 18h, and prepared for luminescence or microscopy. Correlation between the number of syncytia counted by microscopy (n=10 per condition) and the luciferase activity was determined, and the calculated correlation coefficient is R^2=0.87.

SI-Figure 7: **Secretion of S1.** HeLa cells were transiently co-expressed with double-tagged spike protein (N-terminal HA-tag; C-terminal V5-tag), WT (S) or its mutants, µS1/S2 or µAS1/S2, and ACE2 alone or in combination with TMPRSS2, WT (TMPRSS2) or its S441A active-mutant (µTMPRSS2), at a ratio S:ACE2:TMPRSS2 = 1:0.5:0.5. Immunoblot of the 24h conditioned media was first probed for secreted S1, S1' and $S1_L$ (HA-HRP antibody), stripped and next probed for shed ACE2 (sACE2).

Figure 1

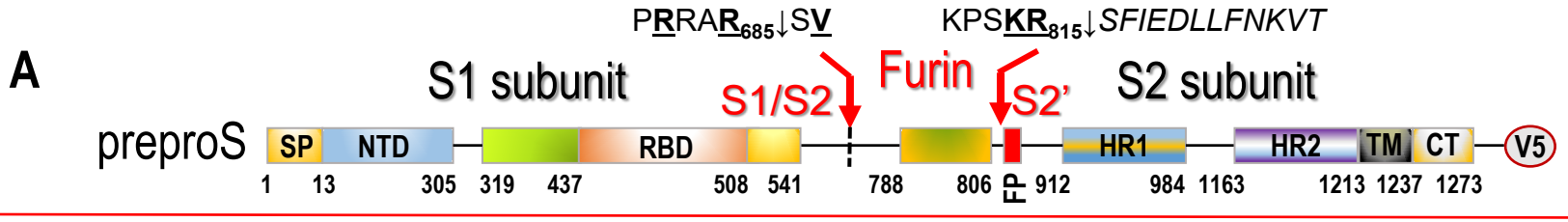
A
PRRAR685↓SV
KPSKR815↓SFIEDLLFNKVT
S1 subunit
S1/S2
Furin
S2'
S2 subunit
preproS
SP
NTD
RBD
FP
HR1
HR2
TM
CT
V5
1
13
305
319
437
508
541
788
806
912
984
1163
1213
1237
1273

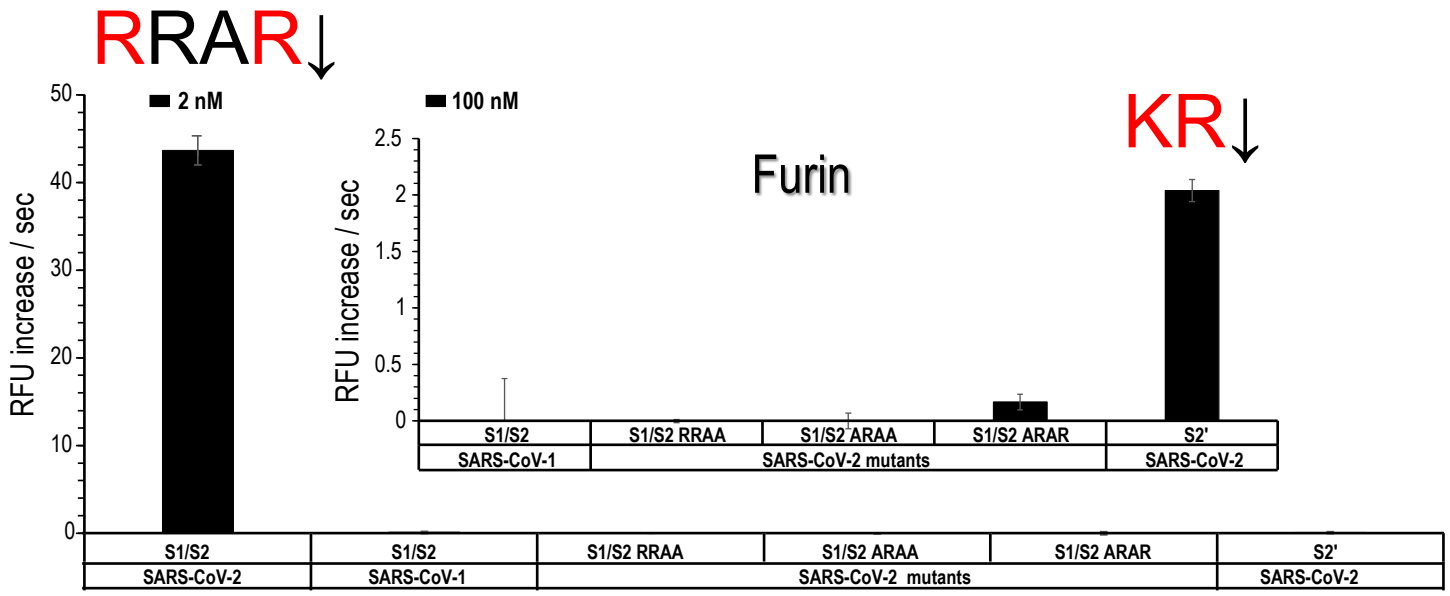
B
RRAR↓
2 nM
RFU increase / sec
100 nM
Furin
KR↓
S1/S2
SARS-CoV-2
S1/S2
SARS-CoV-1
S1/S2 RRAA
S1/S2 ARAA
S1/S2 ARAR
SARS-CoV-2 mutants
S2'
SARS-CoV-2

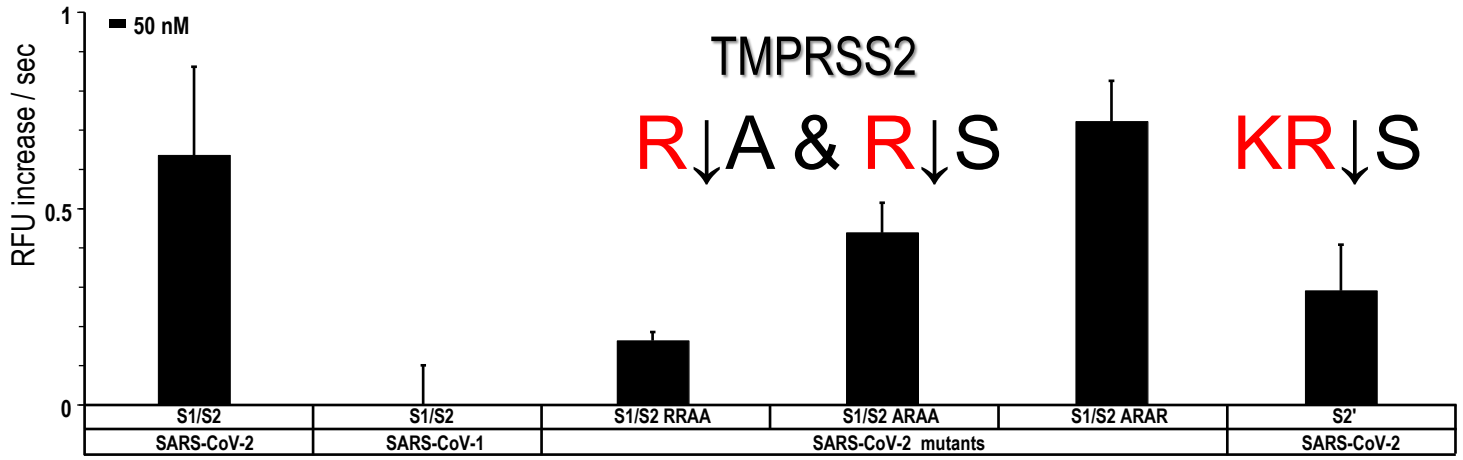
C
50 nM
RFU increase / sec
TMPRSS2
R↓A & R↓S
KR↓S
S1/S2
SARS-CoV-2
S1/S2
SARS-CoV-1
S1/S2 RRAA
S1/S2 ARAA
S1/S2 ARAR
SARS-CoV-2 mutants
S2'
SARS-CoV-2

Figure 1: **Processing of S-peptides by Furin and TMPRSS2.** (**A**) Schematic representation of the primary structure of preproS and its domains and the predicted Furin-like S1/S2 site generating the S1- and S2-subunits, as well as the S2' site preceding the fusion peptide (FP). The signal peptide (SP), N-terminal domain (NTD), receptor binding domain (RBD) to ACE2, the two heptad repeats HR1 and HR2, the transmembrane domain (TM), the cytosolic tail (CT) and the C-terminal V5-tag are indicated. (**B**) *In vitro* Furin activity against peptides mimicking the S1/S2 (and its mutants) and S2' cleavage site sequence of the spike protein from SARS-CoV-2 and SARS-CoV-1, as described in SI-Table 1. Each substrate was tested at a final protease concentration of 2 and 100 nM. (**C**) *In vitro* TMPRSS2 activity (at 50 nM) against peptides mimicking the S1/S2 and S2' cleavage site sequence of the spike protein from SARS-CoV-2 (and its mutants) described in SI-Table 1.

Figure 2

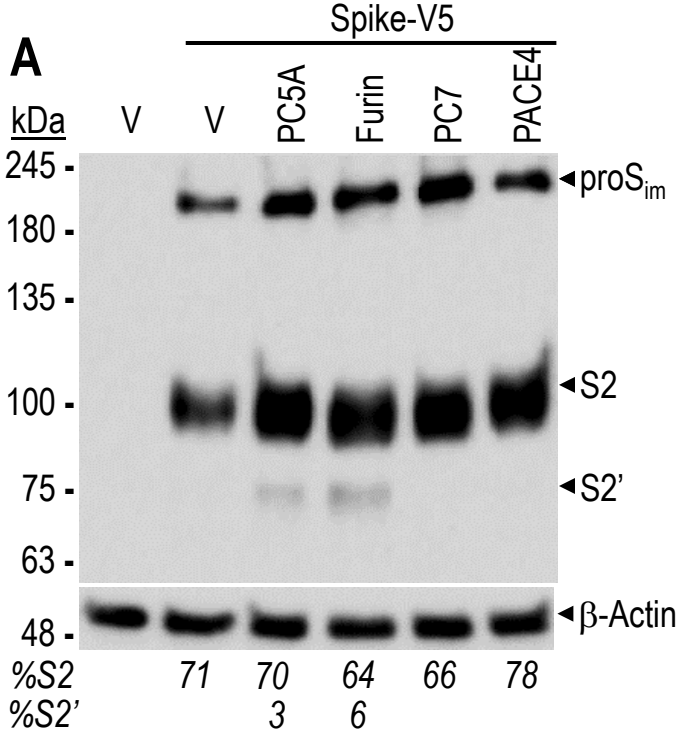
A
Spike-V5
kDa
V
V
PC5A
Furin
PC7
PACE4
245
180
135
100
75
63
48
proS$_{im}$
S2
S2'
β-Actin
%S2
71
70
64
66
78
%S2'
3
6

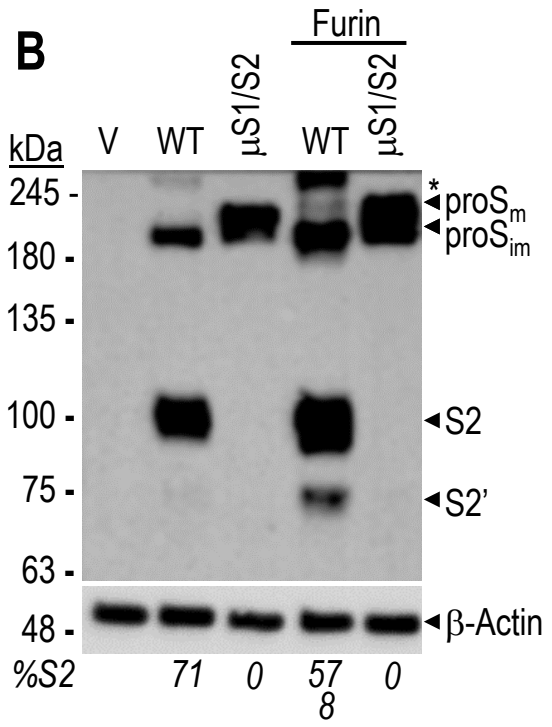
B
Furin
V
WT
μS1/S2
WT
μS1/S2
kDa
245
180
135
100
75
63
48
*
proS$_m$
proS$_{im}$
S2
S2'
β-Actin
%S2
71
0
57
8
0

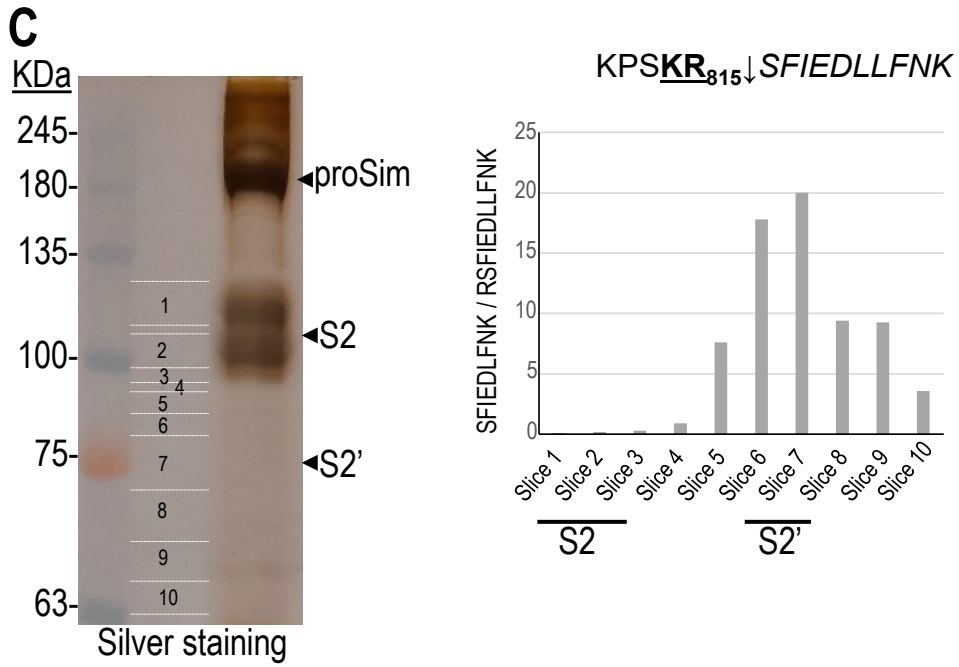
C
KDa
245
180
135
100
75
63
proSim
S2
S2'
1
2
3
4
5
6
7
8
9
10
Silver staining
KPSKR$_{815}$↓SFIEDLLFNK
SFIEDLFNK / RSFIEDLLFNK
25
20
15
10
5
0
Slice 1
Slice 2
Slice 3
Slice 4
Slice 5
Slice 6
Slice 7
Slice 8
Slice 9
Slice 10
S2
S2'

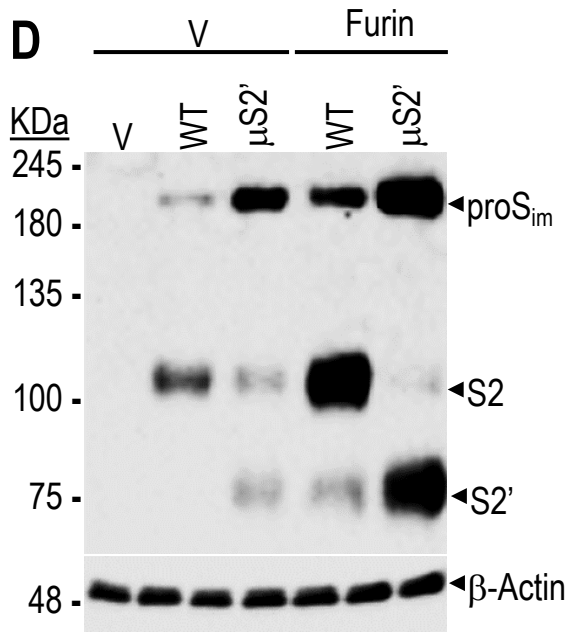
D
V
Furin
kDa
V
WT
μS2'
WT
μS2'
245
180
135
100
75
48
proS$_{im}$
S2
S2'
β-Actin

Figure 2: **Processing of spike-glycoprotein in HeLa cells.** (**A**) Western blot analyses of the processing of WT proS into V5-tagged S2 and S2' by the proprotein convertases Furin, PC5A, PACE4 and PC7 following co-transfection of their cDNAs in HeLa cells. The migration positions of immature proSim, S2 and S2' as well as the β-Actin loading control are emphasized. V = empty pIRES-EGFP-V5 vector. (**B**) Western blot analyses of HeLa cells following co-transfection with cDNAs coding for either WT-S-protein or its double Ala-mutant [R685A + R682A] (μS1/S2) in the absence or presence of Furin cDNA at a ratio S:protease = 1:2. *Inconsistently observed oligomeric forms of proS. (**C**) Identification of S2' cleavage site by MS/MS. WT-spike-glycoprotein was immunoprecipitated from HeLa cells using V5 agarose beads then resolved by SDS electrophoresis SDS/PAGE and subjected to silver staining (left panel); the positions of the slices are indicated (1 to 10). The MS/MS analysis of peptides generated by a Lys-specific protease (K814↓) are indicated; the data represent the ratio of $SFIEDLLFNK_{825}$ to $R_{815}SFIEDLLFNK_{825}$ (right panel). (**D**) Western blot analyses of HeLa cells co-transfected with V5-tagged spike protein, WT (S) or its Furin-optimized S2' ($KRRKR_{815}$↓SF) mutant (μS2'), and empty vector (V) or Furin. (**A**, **B**) The estimated % cleavages into S1/S2 and S2' are shown and were calculated as the ratio of the V5-immunoreactivity of the cleaved form to the sum of all forms. The data are representative of at least three independent experiments.

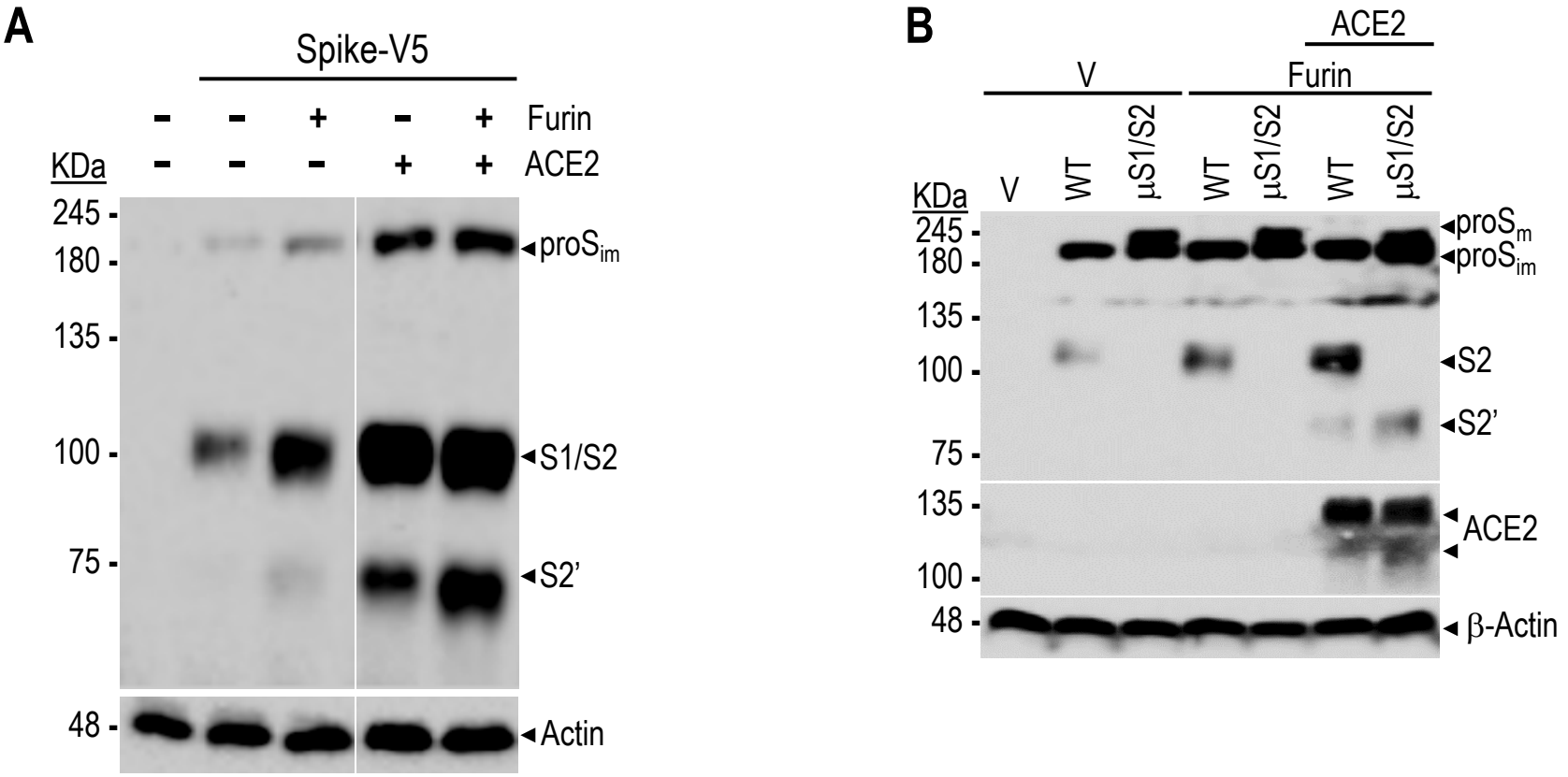
A
Spike-V5
- - + - + Furin
KDa - - - + + ACE2
245
180
135
100
75
48
proS$_{im}$
S1/S2
S2'
Actin
B
ACE2
V
Furin
KDa V WT μS1/S2 WT μS1/S2 WT μS1/S2
245
180
135
100
75
135
100
48
proS$_m$
proS$_{im}$
S2
S2'
ACE2
β-Actin

Figure 3: **Processing of spike-glycoprotein at S2' is enhanced in presence of ACE2.** Western blot showing the impact of ACE2 on the processing of WT and μS1/S2 spike-glycoproteins by Furin. HeLa cells expressing empty vector (V), WT proS (**A**) or its μS1/S2 mutant (**B**) without or with Furin, ACE2 or both were analysed by Western blotting using anti-V5 antibody. The ratio of cDNAs used was S:ACE2:Furin = 1:1:1. The data are representative of at least three independent experiments.

Figure 4

A

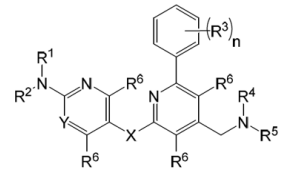

Structure of Furin inhibitors

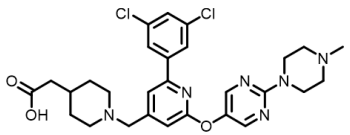

BOS-318

B

	Furin pIC50	PC5 pIC50	PACE4 pIC50	PC7 pIC50
BOS-318	8.8±0.4 (n=10)	6.7±0.15 (n=8)	6.7±0.15 (n=6)	7.4±0.22 (n=8)
BOS-981	9.3±0.5 (n=10)	7.5±0.22 (n=10)	6.9±0.1 (n=4)	6.9±0.2 (n=8)
BOS-857	9.4±0.3 (n=10)	7.6±0.2 (n=10)	6.7±0.24 (n=5)	6.9±0.3 (n=8)
decanoyl-RVKR-cmk	9.1±0.43 (n=447)	9.9±0.38 (n=162)	9.2±0.24 (n=214)	9.6±0.63 (n=198)

C

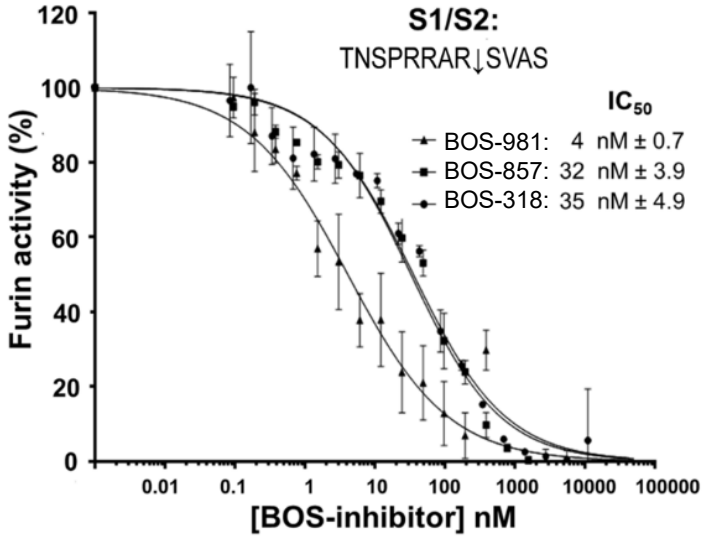

D

	Golgi pIC50 (U20S)
BOS-318	7.7±0.24 (n=22)
BOS-981	8.3±0.25 (n=12)
BOS-857	7.6±0.2 (n=12)
decanoyl-RVKR-cmk	5.1±0.33 (n=8)

E

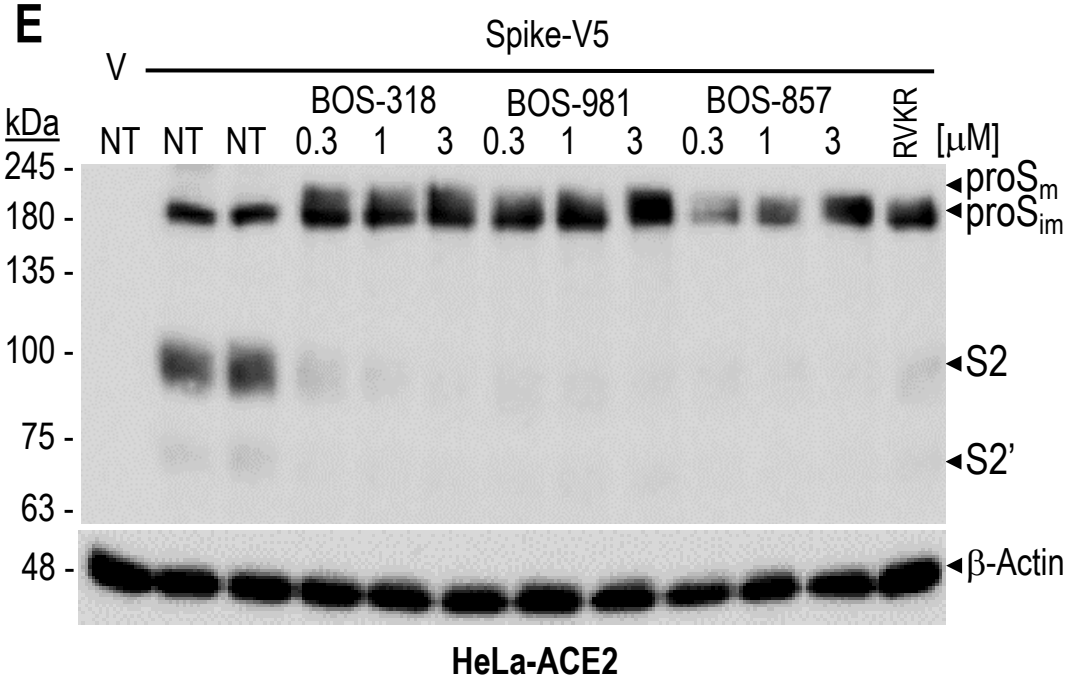

Figure 4: **Inhibition of PCs by BOS compounds.** (**A**) Chemical motif of BOS-inhibitors and representative structure of BOS-318. (**B**) *In vitro* BOS-inhibition of the cleavage of the fluorogenic dibasic substrate FAM-QRVRRAVGIDK-TAMRA by each of the proprotein convertases Furin, PC5 (PCSK5), PACE4 (PCSK6) and PC7 (PCSK7). All experiments were performed in 10 different wells and the average pIC_{50} (in nM) was calculated. Shown for comparison is the inhibitory pIC_{50} of the Furin-like inhibitor dec-RVKR-cmk performed >100 times. (**C**) *In vitro* inhibition of Furin by the BOS compounds. Furin (2 nM) was incubated with increasing concentration of BOS-inhibitors, and its enzymatic activity against the synthetic peptides DABSYL/Glu-TNSP**RR**A**R**↓SVAS-EDANS (5 μM) was measured at pH 7.5 (n=3). (**D**) Golgi assay: table representing the effects of BOS-inhibitors on U2OS cells expressing each of Furin, PC5A, PACE4 and PC7 simultaneously transduced with a BacMam-delivered construct containing a Golgi-targeting sequence followed by a 12-amino acid Furin/PCSK cleavage site from Bone Morphogenic Protein 10 (BMP10) and GFP at the C terminus (GalNAc-T2-GGGGS-DSTARIRR↓NAKG-GGGGS-GFP). Dibasic cleavage releases NAKG-GGGGS-GFP thereby reducing the Golgi-associated fluorescence estimated by imaging. (**E**) Furin-inhibitors (BOS) abrogate endogenous processing of the spike-glycoprotein. Hela cells were transiently transfected with a cDNA encoding an empty vector (V) or with one expressing the V5-tagged spike (S) glycoprotein (spike-V5). At 5h pre-transfection, cells were treated with vehicle DMSO (NT, duplicate) or with the Furin-inhibitors at indicated concentrations, or RVKR-cmk at 50 μM. At 24h post-transfection media were replaced with fresh ones lacking (NT) or containing the inhibitors for an additional 24h. Cell extracts were analyzed by Western blotting using a mAb-V5. All data are representative of at least three independent experiments.

Figure 5

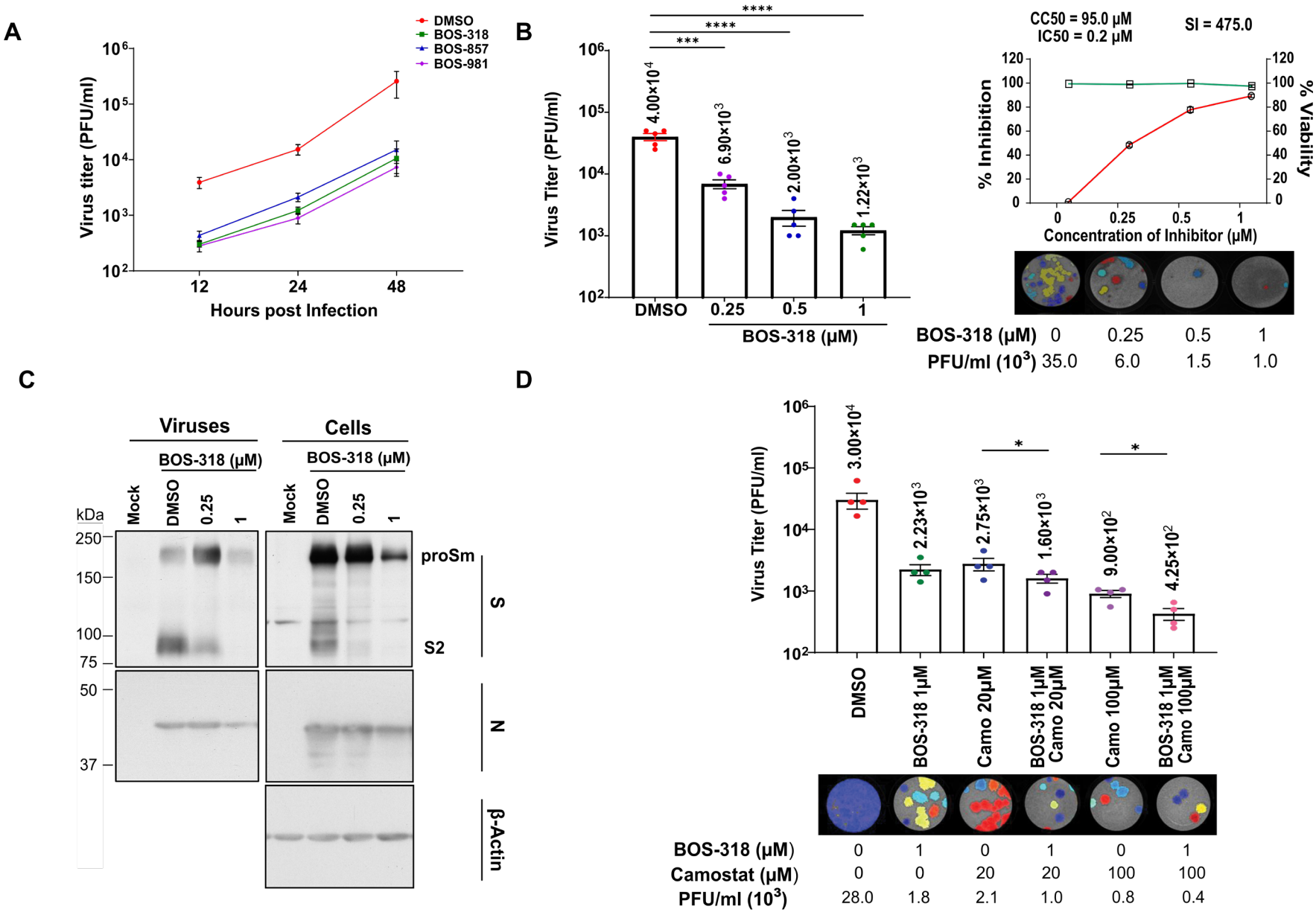
A
DMSO
BOS-318
BOS-857
BOS-981
Virus titer (PFU/ml)
Hours post Infection
B
Virus Titer (PFU/ml)
4.00×10^4
6.90×10^3
2.00×10^3
1.22×10^3
DMSO
0.25
0.5
1
BOS-318 (μM)
CC50 = 95.0 μM
IC50 = 0.2 μM
SI = 475.0
% Inhibition
% Viability
Concentration of Inhibitor (μM)
BOS-318 (μM) 0 0.25 0.5 1
PFU/ml (10^3) 35.0 6.0 1.5 1.0
C
Viruses
Cells
BOS-318 (μM)
Mock
DMSO
0.25
1
kDa
250
150
100
75
50
37
proSm
S2
S
N
β-Actin
D
Virus Titer (PFU/ml)
3.00×10^4
2.23×10^3
2.75×10^3
1.60×10^3
9.00×10^2
4.25×10^2
DMSO
BOS-318 1μM
Camo 20μM
BOS-318 1μM Camo 20μM
Camo 100μM
BOS-318 1μM Camo 100μM
BOS-318 (μM) 0 1 0 1 0 1
Camostat (μM) 0 0 20 20 100 100
PFU/ml (10^3) 28.0 1.8 2.1 1.0 0.8 0.4

Figure 5: **Furin-like inhibitors and Camostat treatment decrease SARS-CoV-2 infection in Calu-3 Cells.** (**A**) Replication kinetics was studied at 12, 24 and 48h post-infection by plaque assay to determine PFUs of SARS-CoV-2 virus in the supernatant of infected Calu-3 cells treated or not with 1μM BOS-318, BOS-857 and BOS-981. A line graph represents results of the triplicate plaque assay results (mean ± SD). (**B**) The virus titers (PFU per milliliter) released in the supernatant (24h post-infection) of infected Calu-3 cells treated with indicated concentrations of BOS-318 were determined by plaque assay (mean ± SD of triplicates, *$p < 0.05$; **$p < 0.01$; ***$p < 0.001$) (left panel). The selectivity index (SI) of BOS-318 in Calu-3 cells as shown in top right panel was determined by CC_{50}/IC_{50}. The left y axis indicates the inhibition of virus titer (percent) relative to that of the untreated control group (red). The right y axis indicates the cell viability (percent) relative to that of the untreated control group (green). The CC_{50} (50% cytotoxic concentration), IC_{50} (half maximal inhibitory concentration), and SI (selectivity index) values for each inhibitor are as shown. Representative plaque images of infected Calu-3 cells treated with indicated doses of BOS-inhibitors are shown in the bottom right panel. (**C**) Immunoblots for the infected Calu-3 cells (right panel) and viral particles secreted in the supernatant (left panel) with and without treatment with BOS-inhibitors indicate reduced viral protein levels. Immunoblots were probed for the full-length (proSm) and cleaved (S2) fragments of viral S protein and nucleocapsid (N) protein as indicated; β-Actin was included as the loading control for the cells. (**D**) The virus titers (PFU per milliliter) released in the supernatant (24h post-infection) of infected Calu-3 cells treated with BOS-318 and/or Camostat (Camo) were determined by plaque assay (mean ± SD of duplicates, *, $p < 0.05$; **, $p < 0.01$; ***, $p < 0.001$) (top panel). Representative plaque images of infected Calu-3 cells are shown in the bottom panel. Color plaques differentiate the lawn (one color gray per well) from individual plaques (independent colors).

Figure 6

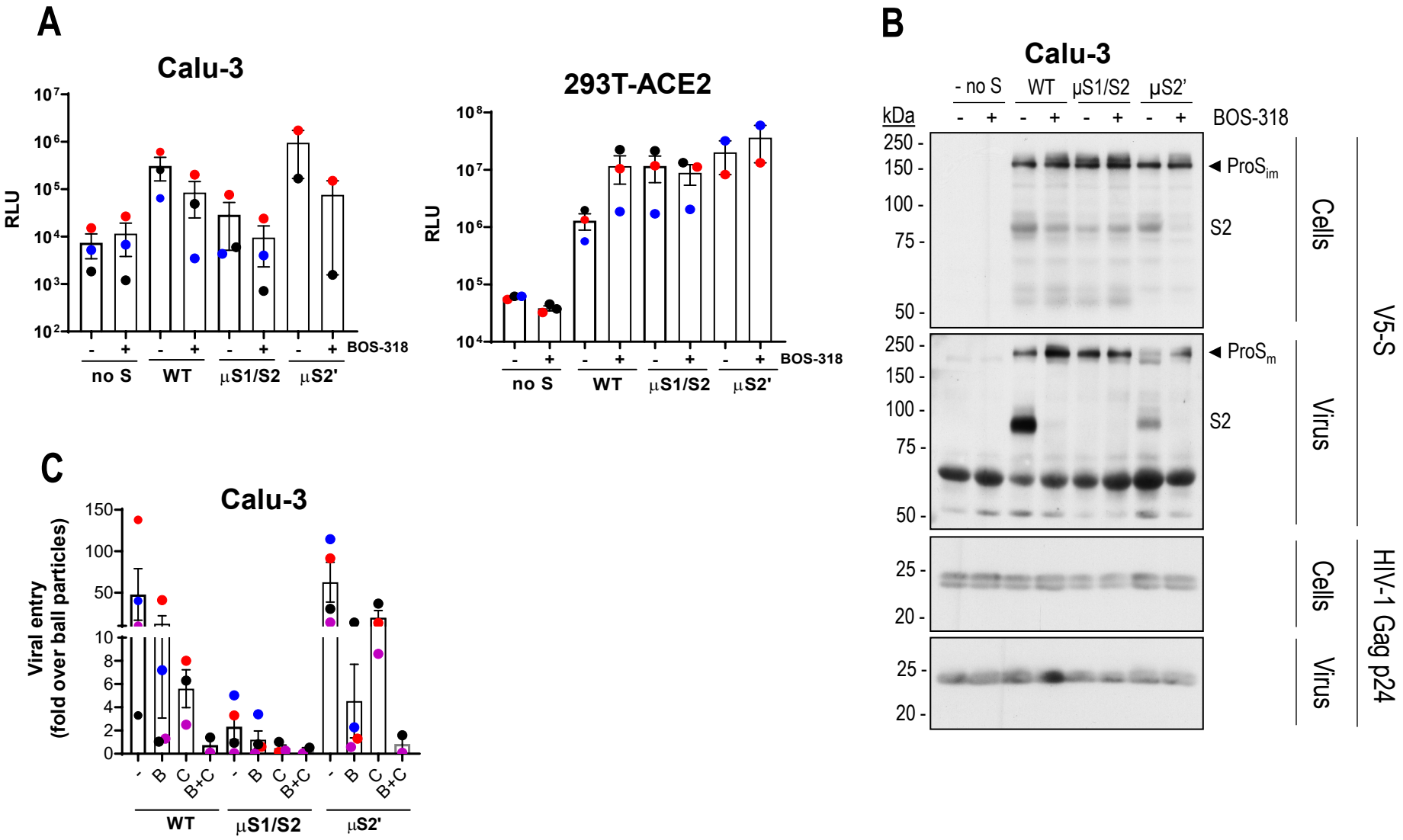
A
Calu-3
RLU
BOS-318
no S
WT
μS1/S2
μS2'
293T-ACE2
B
Calu-3
- no S
WT
μS1/S2
μS2'
kDa
BOS-318
ProSim
S2
ProSm
Cells
Virus
V5-S
HIV-1 Gag p24
C
Calu-3
Viral entry
(fold over ball particles)
WT
μS1/S2
μS2'

Figure 6: **Processing of SARS-CoV-2 S by Furin-like convertases and TMPRSS2 is critical for viral entry in human lung epithelial cells but not in model HEK293 cells stably expressing ACE2**. (**A**) Furin cleavage of proS at the S1/S2 site is required for SARS-CoV-2 pseudoviral entry in Calu-3 cells but not HEK293T-ACE2 cells. Cells were inoculated with nanoluciferase-expressing HIV particles pseudotyped with SARS-CoV-2: wild-type spike (WT), double Ala-mutant spike (μS1/S2) or Furin-optimized spike (μS2'). Inhibition of proS processing at S1/S2 by a novel Furin-like inhibitor (BOS-318) during pseudovirion packaging prevents viral entry in Calu-3 cells but not in HEK293T-ACE2 cells. (**B**) Western blot analyses show inhibition by BOS-318 of proS processing at S1/S2 site. Purified pseudovirions and cellular extracts of producing HEK293-T17 cells treated or not with BOS-318 inhibitor were separated on SDS-PAGE gel and analyzed for HIV-1 p24 and V5-tagged S-protein (proSm or cleaved, S2) as indicated. (**C**) Pre-treatment of Calu-3 cells with 1 μM BOS-318 (B), 100 μM Camostat (C) or both (B+C) markedly reduces viral entry. In Panels A and C, Calu-3 cells were transduced with nanoluciferase-expressing HIV particles pseudotyped with SARS-CoV-2 S WT, μS1/S2 or μS2' for 72h and analyzed for nano-luciferase expression. Viral entry was expressed as fold increase over that given by bald particles (pseudovirions made in the absence of S). Each dot represents a different experiment with median luciferase activity calculated from three biological replicates. Two to four experiments were performed for each cell type. Error bars indicate standard deviation (SD) from the mean.

A

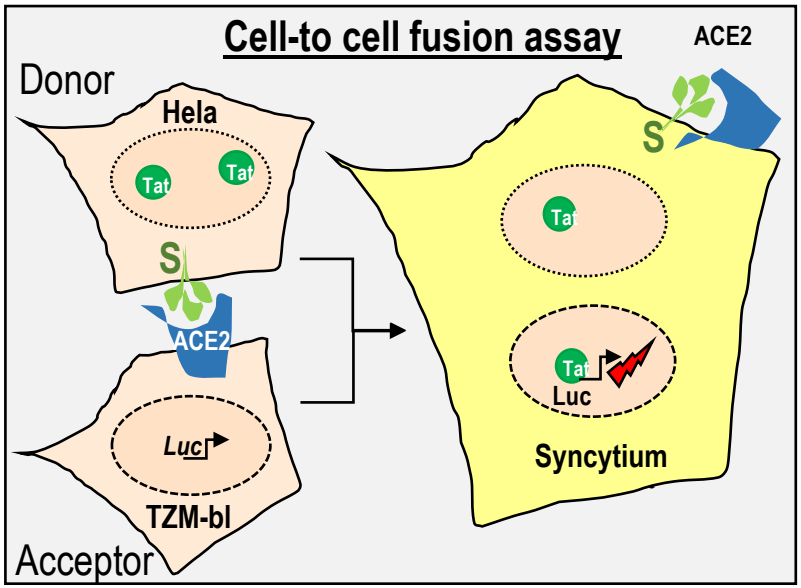
Cell-to cell fusion assay
ACE2
Donor
Hela
Tat
Tat
S
ACE2
Luc
TZM-bl
Acceptor
S
Tat
Tat
Luc
Syncytium

B

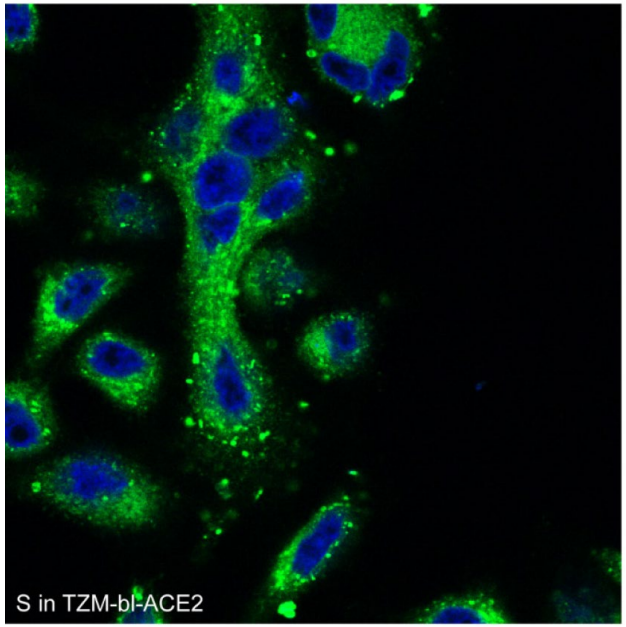
S in TZM-bl-ACE2

C

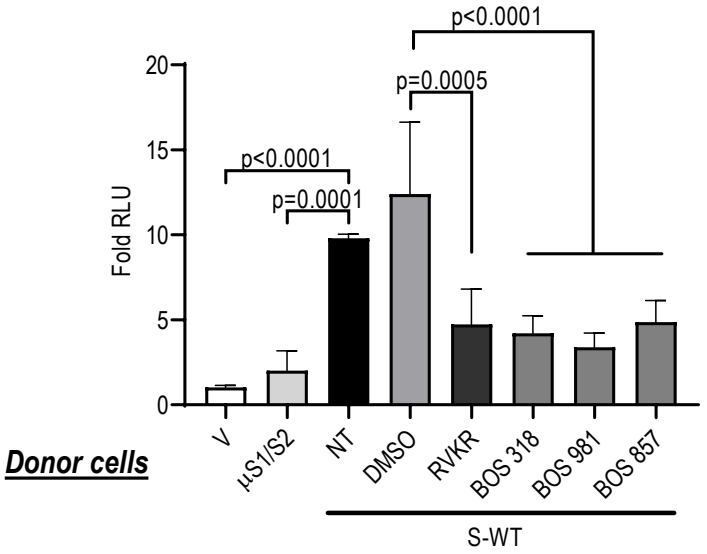
ACE2 in acceptor cell
p<0.0001
p=0.0005
p<0.0001
p=0.0001
Fold RLU
20
15
10
5
0
V
µS1/S2
NT
DMSO
RVKR
BOS 318
BOS 981
BOS 857
Donor cells
S-WT

D

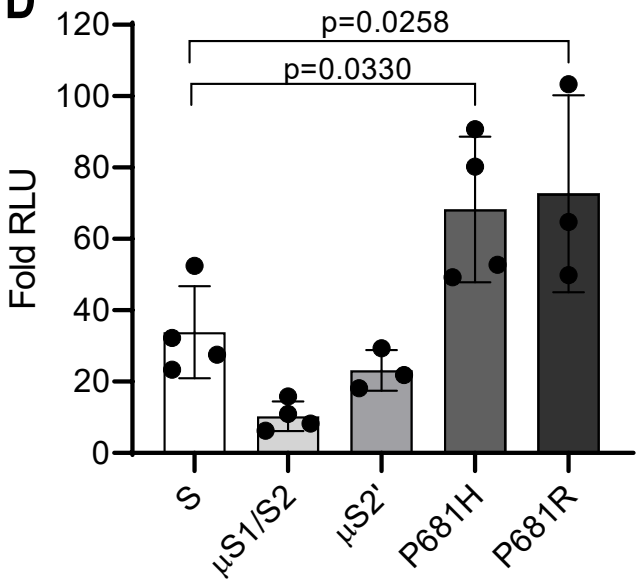
p=0.0258
p=0.0330
Fold RLU
120
100
80
60
40
20
0
S
µS1/S2
µS2'
P681H
P681R

Figure 7: **Spike-induced cell-to-cell fusion relies on Furin cleavage at S1/S2.** (**A**) Cell-to-cell fusion between donor cells (HeLa) expressing the fusogenic SARS-CoV-2 spike protein along with the HIV trans-activator Tat, and acceptor cells (TZM-bl) that express ACE2. Upon fusion, Tat is transferred from donor to acceptor cells, thereby inducing luciferase expression. (**B**) Cell-to-cell fusion was evaluated using confocal microscopy. A representative immunocytochemistry of Hela cells transfected with a vector expressing SARS-CoV-2 spike co-cultured with TZM-bl cells for 18h. The number of syncytia (multiple nuclei) was examined using CellMask™ to probe for the plasma membrane and Dapi to stain the nuclei. (**C**) Donor cells were transfected with vectors expressing either no protein (empty vector, V), μS1/S2, or WT-spike (S) in the absence (NT) or presence of vehicle (DMSO) or with the Furin-inhibitors BOS-318, BOS-981, BOS-857 (300 nM) or RVKR (10 μM). Acceptor cells were transfected with a vector expressing ACE2. After 48h, donor and acceptor cells were co-cultured for 18h. Relative luminescence units (RLU) were normalized to the V value arbitrarily set to 1. Data are presented as mean values ± SD (n=3), One-Way ANOVA, Dunn-Sidàk multiple comparison test. (**D**) Donor HeLa cells expressing WT-S or its indicated mutants and variants were co-cultured with acceptor TZM-bl cells expressing ACE2. The extent of fusion is represented as a ratio between the RLU measured for each condition and that of donor cells expressing empty vector. The bar graph represents the average of 4 experiments performed in triplicates. Data are presented as mean values ± SEM (n=3 or 4), One-way Anova Dunnett's multiple comparison test.

Figure 8

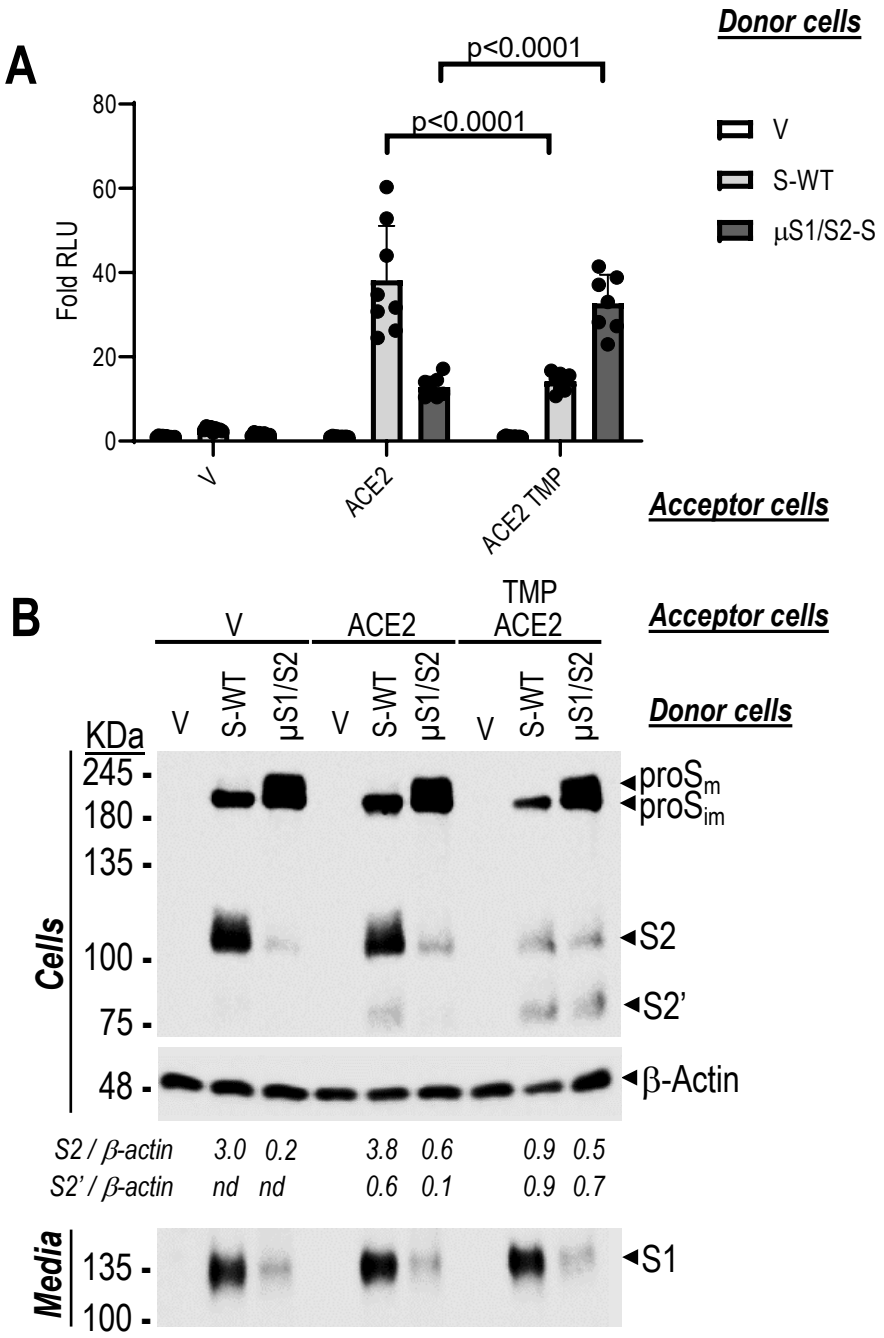
A
Donor cells
p<0.0001
p<0.0001
80
60
40
20
0
Fold RLU
V
S-WT
μS1/S2-S
V
ACE2
ACE2 TMP
Acceptor cells
B
Acceptor cells
V
ACE2
TMP ACE2
V
S-WT
μS1/S2
V
S-WT
μS1/S2
V
S-WT
μS1/S2
Donor cells
KDa
245
180
135
100
75
48
Cells
proSm
proSim
S2
S2'
β-Actin
S2 / β-actin 3.0 0.2 3.8 0.6 0.9 0.5
S2' / β-actin nd nd 0.6 0.1 0.9 0.7
Media
135
100
S1

Figure 8: **Spike-glycoprotein processing by Furin and TMPRSS2 in a co-culture system and their role in cell-to-cell fusion.** Donor HeLa cells expressing empty vector (V), WT-S-HA or μS1/S2-HA were co-cultured with acceptor TZM-bl cells expressing V, ACE2 + V, or ACE2 + TMPRSS2. From the same experiment, cell-to-cell fusion (**A**) was assessed in parallel with spike processing in cells and media by Western blotting (**B**). (**B**) spike-glycoproteins in the cell extracts were analyzed by Western blotting using an anti-V5 mAb. Secreted forms of spike protein (S1) in the media were detected with anti HA-HRP upon immunoprecipitation with anti-HA agarose. The bar graph represents the average of 3 experiments performed in triplicates. Data are presented as mean values ± SD Two-way Anova Turkey's multiple comparison test. The corresponding Western-blot is representative of three independent experiments. Values of S2 and S2' relative to β-actin are shown (nd = too low or not detected).

Figure 9

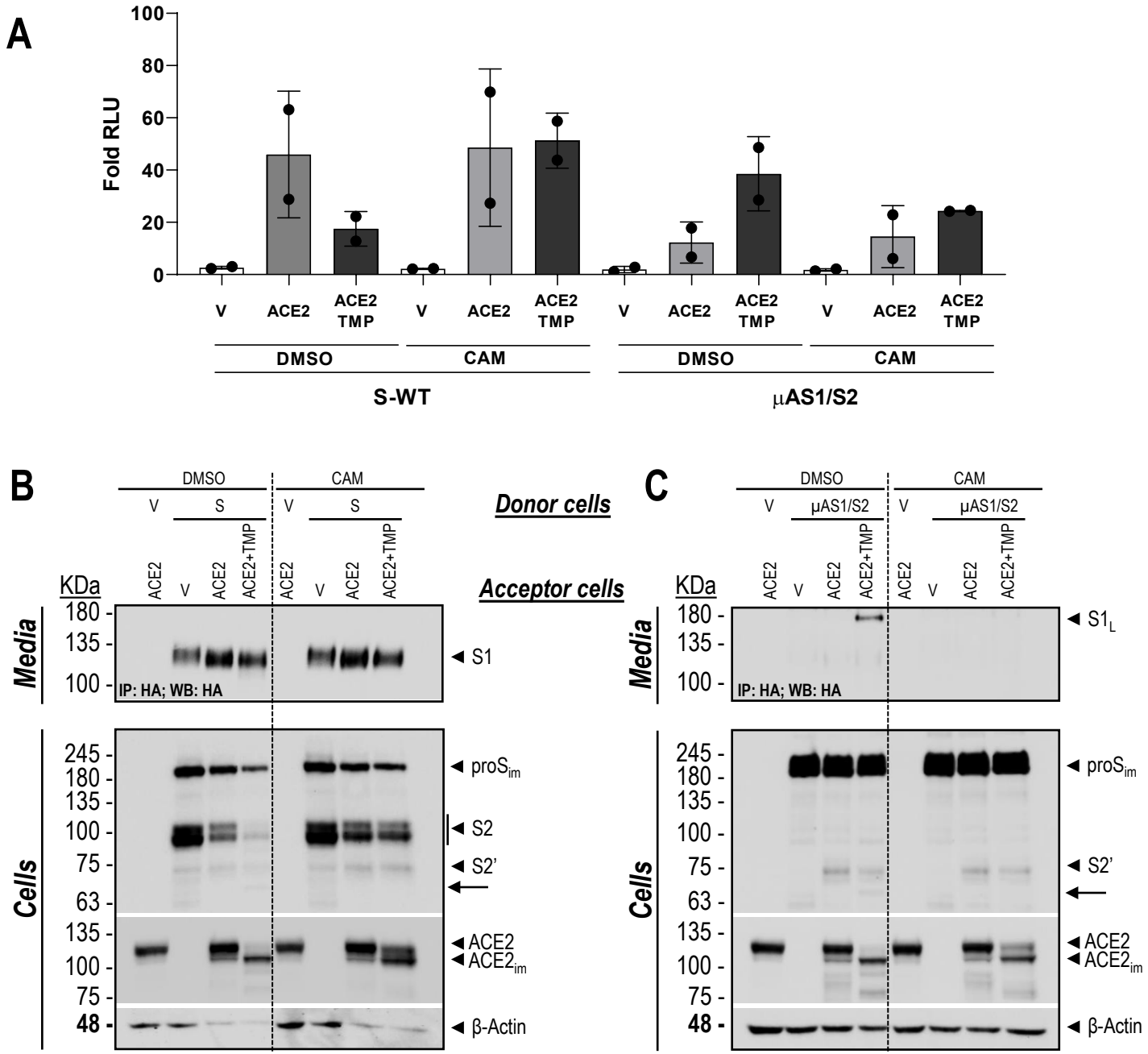
A
Fold RLU
100
80
60
40
20
0
V
ACE2
ACE2 TMP
DMSO
CAM
S-WT
μAS1/S2
B
C
Donor cells
Acceptor cells
KDa
Media
Cells
IP: HA; WB: HA
S1
S1L
proSim
S2
S2'
ACE2
ACE2im
β-Actin
180
135
100
245
75
63
48

Figure 9: **Exogenous TMPRSS2-generated shedding of ACE2 differentially regulates S-induced fusion at the plasma membrane of WT-S *versus* μAS1/S2.** Donor HeLa cells expressing double tagged (N-terminal HA-tag; C-terminal V5-tag) spike-glycoprotein WT (S) or its S1/S2 mutant (μAS1/S2) were co-cultured with acceptor TZM-bl cells expressing (empty vector, V), ACE2 + V, or ACE2 + TMPRSS2 and treated with DMSO (vehicle control) or Camostat (120μM). Within the same experiment, cell-to-cell fusion (**A**) was assessed in parallel with spike processing in cells and media by Western-blot (**B, C**). (**A**) The extent of fusion is represented as a ratio between the RLU measured for each condition and that of donor cells expressing V. The bar graph represents the average of 2 experiments performed in triplicates. (**B, C**). Western blot analyses of media and cell extracts of the co-cultured cells with donor cells overexpressing double tagged (N-terminal HA-tag; C-terminal V5-tag) spike-glycoprotein, WT (S) (**B**) or μAS1/S2 (**C**). The arrow points to a putative degradation product of S2', that is absent in presence of Camostat. Media were subjected to immunoprecipitation with anti-HA agarose for the secreted forms of spike protein (S1, $S1_L$) followed by Western blotting with anti HA-HRP. spike-glycoproteins in the cell extracts were immunoblotted with anti-V5 mAb. The data are representative of three independent experiments.

Figure 10

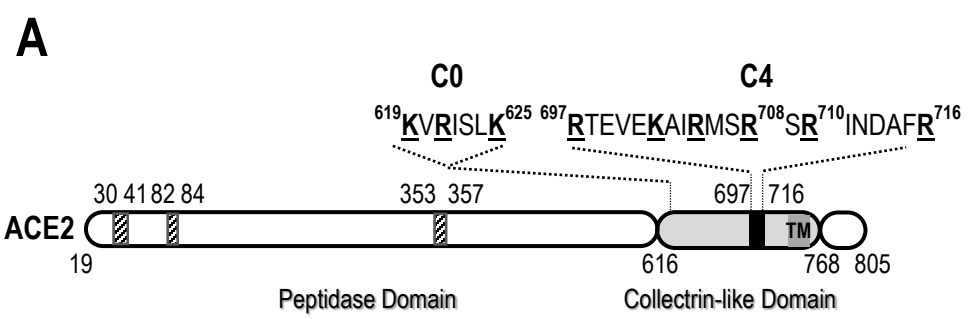
A
C0
C4
619KVRISLK625 697RTEVEKAIRMSR708SR710INDAFR716
30 41 82 84
353 357
697 716
ACE2
TM
19
616
768 805
Peptidase Domain
Collectrin-like Domain

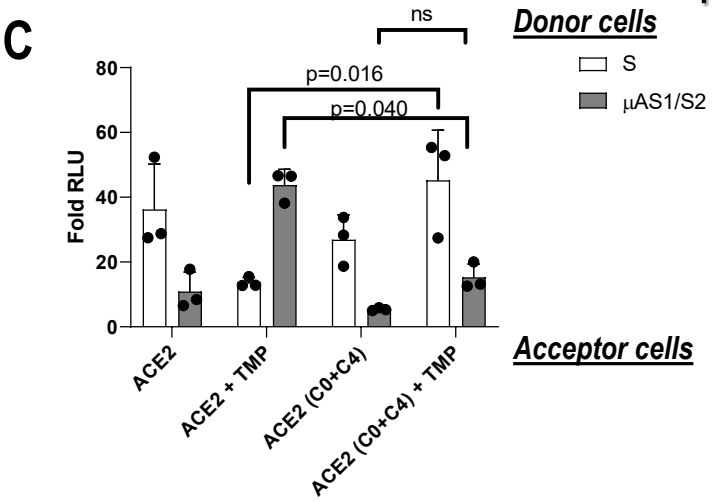
C
ns
Donor cells
S
μAS1/S2
p=0.016
p=0.040
Fold RLU
80
60
40
20
0
ACE2
ACE2 + TMP
ACE2 (C0+C4)
ACE2 (C0+C4) + TMP
Acceptor cells

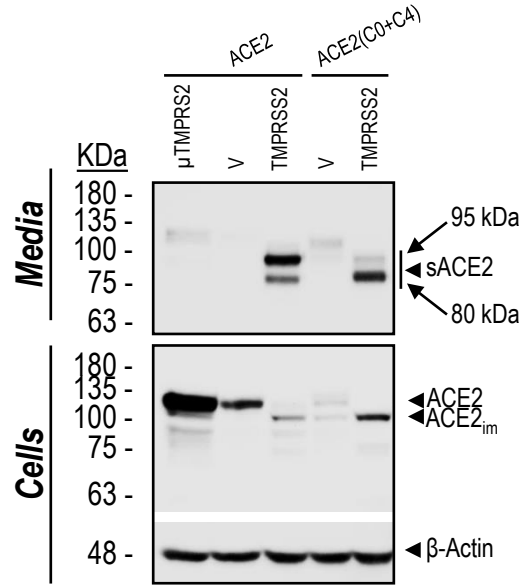
B
ACE2
ACE2(C0+C4)
μTMPRS2
V
TMPRSS2
V
TMPRSS2
KDa
Media
180 -
135 -
100 -
75 -
63 -
95 kDa
sACE2
80 kDa
Cells
180 -
135 -
100 -
75 -
63 -
48 -
ACE2
ACE2im
β-Actin

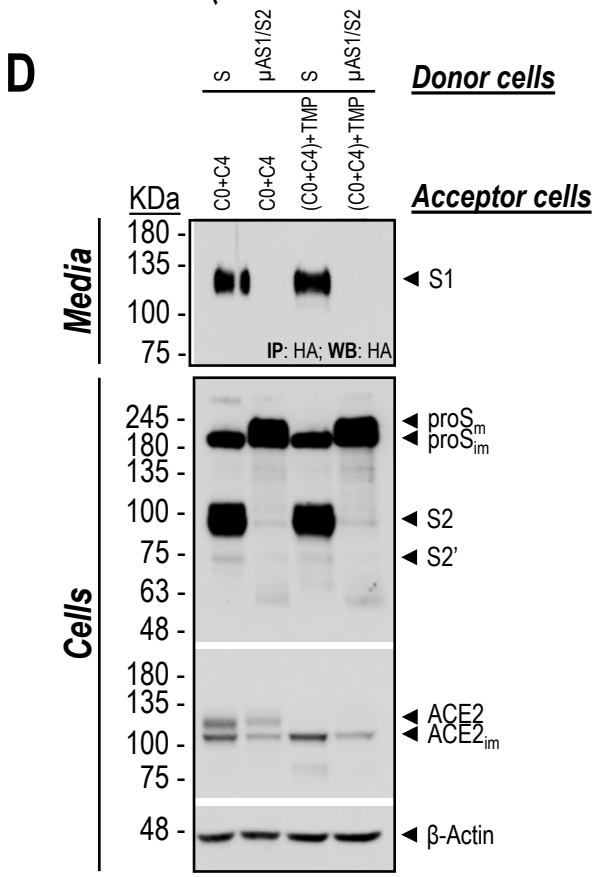
D
S
μAS1/S2
S
μAS1/S2
Donor cells
C0+C4
C0+C4
(C0+C4)+TMP
(C0+C4)+TMP
Acceptor cells
KDa
Media
180 -
135 -
100 -
75 -
S1
IP: HA; WB: HA
Cells
245 -
180 -
135 -
100 -
75 -
63 -
48 -
proSm
proSim
S2
S2'
180 -
135 -
100 -
75 -
48 -
ACE2
ACE2im
β-Actin

Figure 10: **The C-terminal collectrin-like domain of ACE2 may be critical for the regulation of cell-to-cell fusion of spike-glycoprotein when exogenous TMPRSS2 is present.** (**A**) Schematic representation of the primary structure of human ACE2 with emphasis on the C-terminal collectrin-like domain (aa 616-768, light grey), TMPRSS2 cleavage region (aa 697-716, black) and the polybasic amino-acid segments in which K/R were mutated to A (C0 and C4) (amino acids underlined and in bold). Also shown are the peptidase domain (aa 19-615, white) containing the regions involved in the interaction with the spike SARS-CoV protein (hatched) and transmembrane domain (TM). (**B**) HeLa cells were co-transfected with ACE2, WT (ACE2) or its mutant ACE2 (C0+C4), and TMPRSS2, WT (TMPRSS2) or its S441A active-site mutant (μTMPRSS2), or empty vector (V). Media and cell extracts were analyzed by western blotting for shed ACE2 (sACE2) and ACE2, respectively. The migration positions of the ~95 kDa and ~80 kDa sACE2 are emphasized. (**C**) Donor HeLa cells expressing WT-S-HA or μAS1/S2-HA were co-cultured with acceptor TZM-bl cells expressing ACE2, WT (ACE2) or its mutant ACE2 (C0+C4) in presence or absence of TMPRSS2. From the same experiment, cell-to-cell fusion was assessed (**C**), in parallel with WB analyses of cells and media (**D**). The extent of fusion is represented as a ratio between the RLU measured for each condition and that of donor cells expressing an empty vector. The bar graph represents the average of 3 experiments performed in triplicates. Data are presented as mean values ± SD (n=3), One-way Anova Turkey's multiple comparison test. (**D**) Co-culture media were subjected to immunoprecipitation with anti-HA agarose for the secreted forms of spike protein (S1) followed by western blot with anti HA-HRP. spike-glycoproteins in the cell extracts were immunoblotted with anti-V5 mAb. The Western blot data are representative of three independent experiments.

Figure 11

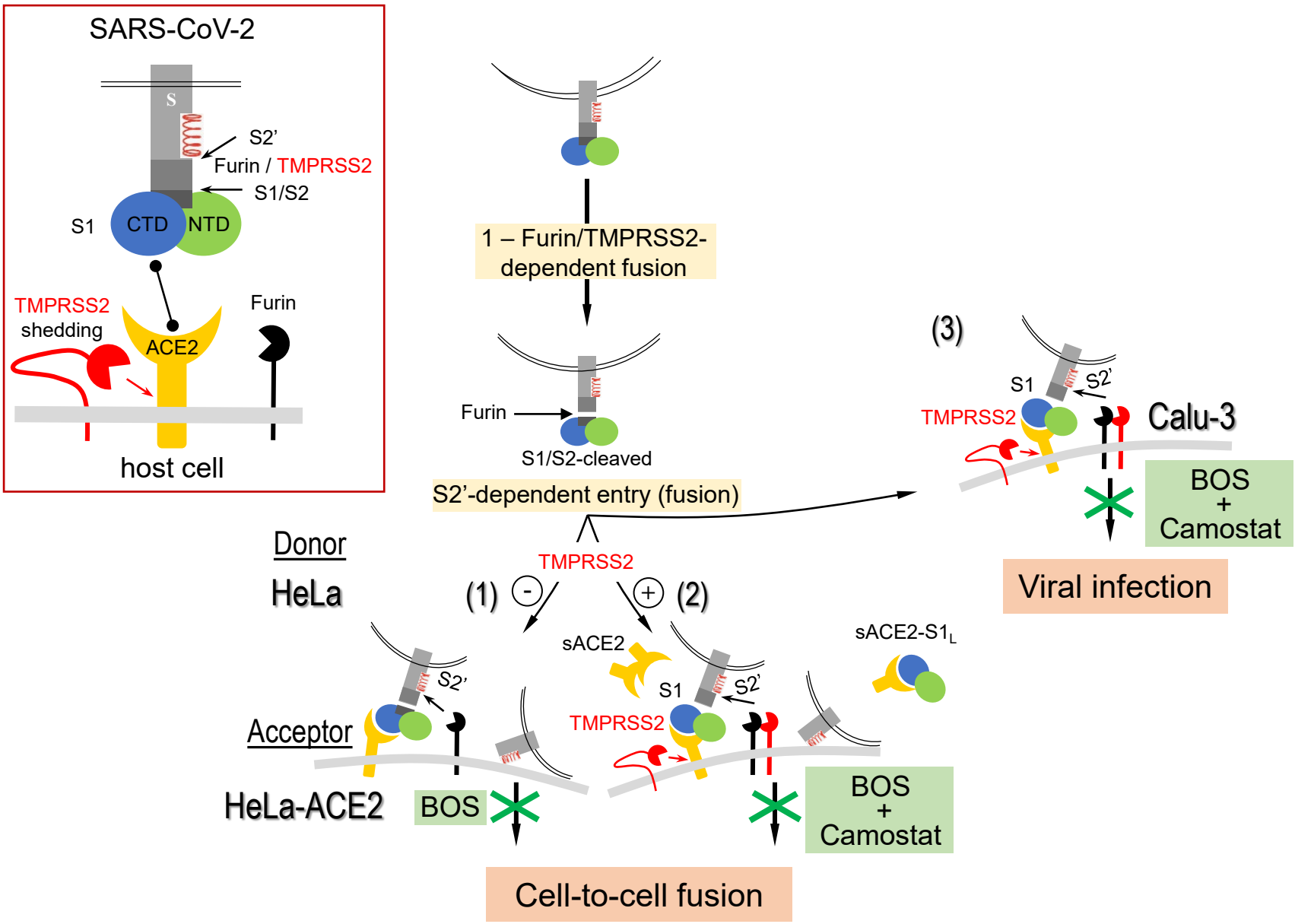
SARS-CoV-2
S
S2'
Furin / TMPRSS2
S1/S2
S1
CTD
NTD
TMPRSS2
shedding
ACE2
Furin
host cell
1 – Furin/TMPRSS2-dependent fusion
Furin
S1/S2-cleaved
S2'-dependent entry (fusion)
(3)
S1
S2'
TMPRSS2
Calu-3
BOS + Camostat
Viral infection
Donor
HeLa
TMPRSS2
(1)
(2)
sACE2
sACE2-S1L
S2'
S1
S2'
TMPRSS2
Acceptor
HeLa-ACE2
BOS
BOS + Camostat
Cell-to-cell fusion

Figure 11: **Proposed model for the processing of S-protein and its blockade by Furin and TMPRSS2 inhibitors.** Boxed left panel: Schematic representation of the S-glycoprotein domains of SARS-CoV-2, including the N-terminal (NTD) and C-terminal (CTD) domains of S1, the Furin-S1/S2 and the Furin/TMPRSS2-S2' processing sites as well as the fusogenic α-helix that follows S2'. Binding of the RBD domain of S1 to the membrane associated ACE2 in target cells, and the cell surface expression of TMPRSS2 and Furin are also schematized. Right panels: **(1)** BOS-inhibitors (or μS1/S2 mutant) completely prevent cell-to-cell fusion of donor Hela cells expressing S-glycoprotein with acceptor HeLa-ACE2 cells, which lack endogenous TMPRSS2. In this context, this reveals that Furin is a major processing enzyme cleaving at S1/S2 and generating S2'. **(2)** In acceptor HeLa cells expressing TMPRSS2 (+), maximal prevention of cell-to-cell fusion can be achieved by a combination of Furin (BOS, phenocopying the μS1/S2 or μAS1/S2 mutants) and TMPRSS2 (Camostat) inhibitors blocks S2' production, ACE2-shedding (sACE2) and the separation of sACE2-S1L complex from S2. **(3)** Optimal blockade of SARS-CoV-2 infection of Calu-3 cells, which express endogenously both Furin and TMPRSS2, is also achieved by a combination of Furin (BOS) and TMPRSS2 (Camostat) inhibitors.